EQC Project 08/550 - Establising a Spatiotemporal Benchmark for Ongoing Crustal Stress Monitoring in the Southern Taupo Volcanic Zone

S. Sherburn
J. Townend
R. Arnold
L. Woods

GNS Science Report 2009/185
July 2009

DISCLAIMER

The data presented in this Report are available to GNS Science for other use from August 2009

BIBLIOGRAPHIC REFERENCE

Sherburn, S.; Townend, J.; Arnold, R.; Woods, L. 2009. EQC Project 08/550 - Establishing a Spatiotemporal Benchmark for Ongoing Crustal Stress Monitoring in the Southern Taupo Volcanic Zone, *GNS Science Consultancy Report* 2009/185. 44p.

CONTENTS

FIGURES

TABLES

EXECUTIVE SUMMARY

We have established the background crustal stress pattern in New Zealand and have developed a method to look for changes in stress with time. Our method could be useful for identifying areas such as the southern Taupo Volcanic Zone that might exhibit stress changes before a volcanic eruption. We first extracted earthquake records from the *GeoNet* earthquake database, and used those data to calculate focal mechanisms which were subsequently used to estimate maximum horizontal stress directions. Stress directions have been estimated for clusters of earthquakes and we have investigated the best methods of determining those clusters. We have investigated the impact of using distance-weighting to down weight focal mechanisms further from cluster centres in an effort to reduce spatial contamination in any temporal changes. For five selected clusters, three in the southern Taupo Volcanic Zone and two control clusters, we have looked for temporal changes in the principal stress directions by dividing the data period into two intervals and comparing “before” and “after”. A statistical test is used to determine the significance of any changes. We have shown that we can detect geophysically significant changes (S_{Hmax} rotations greater than about 30°) with datasets of practicable size (20 or more focal mechanisms).

As a result of the requirements of this study the *GeoNet* project has implemented automatic first motion estimation in the New Zealand earthquake database. This has increased the number of first motions in the database by about 50%. We have also produced more than 600 focal mechanisms for shallow earthquakes, the largest New Zealand dataset of its type that we know of, and 30 S_{Hmax} estimates, also the largest dataset in New Zealand.

INTRODUCTION

Much of the effort put into volcanic eruption forecasting has traditionally focussed on identifying temporal changes in first-order observations such as the level or type of seismicity, the volcanic gas flux, or the extent of ground deformation. At reawakening volcanoes, where magma must intrude to shallow depths before an eruption can occur, such first-order observations may be sufficient to forecast an eruption, but at frequently active volcanoes magma may not have to intrude far and an eruption can occur with little seismicity or ground deformation. The 1995 Mt Ruapehu eruption is an example of such an eruption occurring with little warning (Bryan and Sherburn, 1999; Hurst and McGinty, 1999; Sherburn et al., 1999). In cases like Ruapehu first-order observations may be less useful and a more detailed analysis of the available data may be necessary.

Analysis of temporal changes in the stress field surrounding a volcano is one promising eruption forecasting technique. Such changes have been inferred (after the fact) to have been associated with eruptions at both Mt Spurr in Alaska (Roman et al., 2004) and Montserrat in the Caribbean (Roman et al., 2006), so this technique is at least worth investigating at frequently active New Zealand volcanoes like Ruapehu. Miller and Savage (2001) and Gerst and Savage (2004) used shear-wave splitting observations to indirectly estimate stress directions at Ruapehu and observed changes associated with the 1995 eruption and the post-eruption period. The Ruapehu shear-wave splitting studies used the anisotropic fast direction as a proxy for the axis of maximum horizontal compressive stress, based on the presumption that changes in stress affect populations of cracks governing the rate of shear wave propagation. In comparison, Reyners (2009) compared maximum and minimum horizontal compressive stress directions 15-20 km west of Ruapehu before and after the 1995 eruptions and found no significant change. This throws at least some doubt on the interpretation of Miller and Savage (2001) and Gerst and Savage (2004) that the change in the anisotropic fast direction was due to a stress change, and suggests that a more thorough analysis of stress changes in the southern Taupo Volcanic Zone is warranted in order to interpret the anisotropy data.

This report describes our data and methods, and a set of results applied to a particular subset of data from the *GeoNet* database.

DATA AND METHOD

We explain our method below with respect to three components:

1. Data extraction and pre-processing, and seismograph polarity verification;
2. Stress parameter estimation;
3. Stress change analysis.

Data extraction and pre-processing, and seismograph polarity verification

The *GeoNet* earthquake database contains the parameters of all earthquakes located in New Zealand by the national seismograph network. These data include locations, magnitudes, phase picks, etc, as well as all the data necessary to determine earthquake focal mechanisms. We wrote a Perl script to search the database and extract the parameters required for focal mechanism determinations. The *GeoNet* earthquake database is stored on a GNS Science Oracle database server and the full database is not currently accessible by researchers outside GNS Science. In particular, the data extraction script used here will therefore run only within GNS Science on a computer with the necessary Oracle database support. When the full database becomes accessible outside GNS Science we will make the necessary changes to our data extraction method so that it is available to all researchers.

The database search criteria are given in Table 1. We did not search before 2004 because the seismograph network then was not as dense as it is now and relatively few earthquakes would have satisfied our other criteria. We selected a maximum focal depth of 50 km as we are interested in crustal stress changes. This depth may be too great and this is discussed later. The maximum allowable RMS misfit was selected to eliminate any very poorly located earthquakes, though such events are not likely to satisfy our other criteria. An azimuth gap of 180 ^{o} is a common benchmark beyond which it is considered that earthquakes cannot be well located. A minimum of 10 first motions is a compromise between values used by other authors (Roman et al., 2004, Roman et al., 2006, Sherburn and White 2006). Although the focus of the study is the southern Taupo Volcanic Zone (TVZ) we have assembled data spanning all New Zealand for three reasons:

1. To provide sufficient data with which to develop our techniques, given the relatively small number of focal mechanism data for the southern TVZ;
2. In order to avoid imposing an arbitrary boundary on our analysis;
3. To provide a control dataset spanning a larger proportion of the New Zealand landmass, which can be used by researchers studying other seismotectonic phenomena.

A total of 912 earthquakes met our criteria. At the time the data were extracted, the database was complete for earthquakes larger than magnitude 2.2 (this is an average value for New Zealand and will vary, possibly quite significantly, from place to place), except for a period from about April 2007 to June 2008 for which data processing had not yet been completed. In this incomplete period, only large, possibly felt, earthquakes are assured of inclusion in the database, and only 36 earthquakes during this period met our criterion for the minimum number of first motions (Table 1).

The earthquake phase and first motion data were converted to an input file for FPFIT (Reasenberg and Oppenheimer, 1985), a commonly used program for determining earthquake focal mechanisms. At this stage, first motions from strong-motion seismographs were eliminated from the dataset, as initial tests had indicated that some focal mechanisms were very dependent on data from these instruments whose polarities (correct or reversed) have not been determined. This reduced the number of earthquakes from 912 to 751. Focal mechanisms were determined using FPFIT and excluding multiple solutions. A total of 633 focal mechanisms were determined, ignoring events that did not converge. As far as we are aware, this is the largest dataset of focal mechanisms for shallow New Zealand earthquakes ever assembled. Focal mechanism solutions were converted to the GMT psmeca format (Wessel and Smith, 1991) for plotting and further analysis. The earthquakes and their focal mechanisms are illustrated in Figure 1.

Initial examination of data extracted from the *GeoNet* database revealed fewer first motions than had been anticipated. Subsequent examination of several earthquakes from September 2008, the analysis of which had already been completed, showed that the number of first motions recorded during routine analysis was often many fewer than could be discerned. Following discussions with Kevin Fenaughty (*GeoNet* Data Centre Manager), we decided to attempt to increase the number of first motions by incorporating an automatic first motion picker in the earthquake analysis workflow. An attempt is now made to automatically pick a first motion once manual analysis of each month's earthquakes has been completed, but only for P-phases with assigned qualities of 0 or 1, and only if a first motion has not already been picked manually. As part of developing this automatic first motion picker, the various threshold parameters have been adjusted to ensure optimal agreement between automatic and manual first motion picks. For the dataset used in this study, the addition of automatic first motions has increased the total number of first motions by about 50%.

Seismograph polarity errors (i.e. incorrect wiring) are a major cause of uncertainties in earthquake focal mechanisms and need to be accounted for before focal mechanisms can be reliably calculated. The usual approach to detecting polarity errors is to examine P-phase arrivals from large, teleseismic earthquakes that should have the same first motions at all seismograph locations in New Zealand. We have developed a relatively efficient process for systematically extracting data for earthquakes amenable to instrumental polarity checking. For this study, we automatically extracted a list of earthquakes from the USGS NEIC web page at suitable distances northwest and southeast of New Zealand, calculated the predicted arrival times of those earthquakes in New Zealand and then extracted the appropriate waveform data from the continuous *GeoNet* data archive. Waveform data were examined visually to identify likely polarity errors (Figure 2). Subsequent discussions with Kevin Fenaughty (*GeoNet* Data Centre Manager) revealed that known polarity errors were already corrected in the earthquake database, but to date the known polarity errors and corresponding corrections to the waveform data have not been publicly documented.

As part of the process of checking focal mechanisms before stress parameter estimation, we compared focal mechanisms for larger earthquakes with their moment tensor solutions (Ristau, 2008). In general, there is a good agreement between the two datasets (Figure 3).

Stress parameter estimation

We determine the crustal stress parameters using a methodology similar to that we have used successfully in California, Japan, and the Marlborough region of New Zealand (Townend and Zoback, 2004; Balfour et al., 2005; Townend and Zoback, 2006). The approach consists of first grouping the available focal mechanisms into geographically distinct clusters, and then determining the set of stress parameters most compatible with the focal mechanisms in each cluster.

The focal mechanism data set containing *n* earthquakes is subdivided into *k* clusters on the basis of each earthquake's location using a non-hierarchical clustering algorithm (K-means; Hartigan, 1975) applied to the (weighted) Euclidean distances between all 633 focal mechanisms. This method of clustering is not guaranteed to yield a globally optimum (or even unique) solution, particularly for large-scale clustering problems, but ensures that each earthquake is closer to the centroid of the cluster to which it is assigned than to the centroids of all the other clusters. We have experimented with both two-dimensional and three-dimensional clustering (cf. Balfour et al., 2005; Townend and Zoback, 2006). Since the extent of the catalogue in the horizontal plane greatly exceeds the 50 km maximum depth range, we have examined the effects of scaling the depths by factors of 1, 3, and 9 in the distance calculations and present the results for the intermediate case (×3) here.

We have also experimented with different numbers of clusters, since for K-means clustering this is an *a priori* assumption. We report here on the results obtained using a rule of thumb ('rot') estimate for the number of clusters in a data set of size *n* (Mardia et al., 1979)

$$k_{rot} \approx \sqrt{\frac{n}{2}} \approx 18$$

as well as for a higher number of clusters ($k_{max} = 30$) corresponding to an average of 20 focal mechanisms in each cluster, which previous experience suggests generally yields stable stress estimates (Townend and Zoback, 2006). As the clustering is non-unique, we run the algorithm 50 times from different random starting positions for each choice of k and distance measure (i.e. two- or three-dimensional). We chose the clustering for which the sum over all k clusters of the within-cluster summed centroid-hypocentre distances was a minimum (Townend and Zoback, 2006).

The clustering results are illustrated in Figures 4-6. In these diagrams a line links each focal mechanism to its respective cluster centroid (i.e. the mean position for that cluster).

For the actual stress parameter estimation, we use a recently developed Bayesian algorithm (Arnold and Townend, 2007). This algorithm has been shown to yield the same modal stress parameters as those obtained with a commonly used well-established alternative (Michael, 1987) and to yield posterior uncertainties compatible with an analytical solution (McKenzie, 1969). It further allows weights associated with individual focal mechanisms to be incorporated into the analysis, in our case weighted according to epicentral distance from the cluster centroid. For each cluster of earthquakes, we determine three angular parameters defining the orientations of the three principal stresses (which have magnitudes $S_1 \geq S_2 \geq S_3$) and a fourth parameter known as the stress ratio ($\nu = (S_1 - S_2)/(S_1 - S_3)$), which represents the shape of the stress ellipsoid (that is, the relative magnitude of the three principal stresses). Figure 7 shows an example summary of a stress estimate obtained with the Bayesian method. From the output of the algorithm we derive probability distributions of the directions of the three principal stress directions for each cluster, and display them in stereographic projection. This not only shows the estimated directions, but demonstrates the uncertainties associated with those directions. We can also calculate the probability distributions of the stress ratio, the azimuths of the three principal stress axes and the azimuth of the axis of maximum horizontal compressive stress (discussed below). These probability distributions can be used to create interval estimates known as Bayesian credible intervals (equivalent to confidence intervals).

The stress estimation results are displayed in two ways in this report. We first illustrate the principal stress directions in stereographic projection at each cluster centroid (Figures 8-10). For those clusters containing more than five mechanisms, we also show a plot of the 80% Bayesian credible intervals for the axis of maximum horizontal compressive stress (Figures 11-13).

In cases in which none of the principal stresses is strictly vertical, treating the azimuth of the larger sub-horizontal principal stress as a proxy for the maximum horizontal compressive stress (S_{Hmax}) can introduce directional errors of several tens of degrees (Lund and Townend, 2007). Such errors are likely to be larger than, for instance, temporal variations in stress, and can be avoided using a transformation (Lund and Townend, 2007) that converts the four parameters returned by the inversion algorithm into a robust measure of the axis of maximum horizontal compressive stress, S_{Hmax}. It is common to display S_{Hmax} on maps for easy interpretation, and this method is amenable to computing and illustrating spatiotemporal changes.

If the earthquake focal mechanisms recorded before and after a volcanic eruption or other geological event of interest occur in different places and sample a spatially varying stress field, changes in the corresponding stress parameters will reflect a juxtaposition of spatial and temporal effects (Townend and Zoback, 2001; Townend, 2006). To ameliorate spatial contamination of any temporal stress change signal, we analyse data from different times at a common position using a distance-weighting scheme. The contribution of any focal mechanism to an estimate of the stress tensor at a specific point (the cluster centroid) is weighted according to its epicentral distance from the centroid. Focal mechanisms closer than a distance $r_{\min}$ were given a weight of 1.0, those between $r_{\min}$ and $r_{\max}$ were given a weight decreasing linearly with distance from 1.0 and 0.0, and all focal mechanisms with distances greater than $r_{\max}$ were given a weight of 0.0. For a set of test clusters we carried out the stress inversion holding $r_{\max}$ at 25 km and increasing $r_{\min}$ from 0 to 25 km in steps of 5 km. This was done in order to determine the influence, if any, of more distant focal mechanisms on the derived stress parameters, since these may be driven by a different stress field.

Stress change analysis

If an apparent change in stress orientation with time is observed, the first question to ask is whether the change is significant given estimates of the observational uncertainties. The S_{Hmax} parameter computed from the principal stress orientations and the stress ratio using Lund and Townend's (2007) algorithm is, in statistical terms, a circularly-distributed, non-orientable axis (i.e. the S_{Hmax} and S_{Hmax}+180° directions are equivalent). The associated uncertainty incorporates the effects of the principal stress axes' orientations and the uncertainty in each parameter estimated from focal mechanisms. The Bayesian stress inversion technique yields a full posterior probability distribution for the direction of S_{Hmax}. We can apply the technique to focal mechanisms in the same cluster, but from two successive time periods, and calculate the posterior probability distributions of S_{Hmax}. These probability distributions can then be combined to form the probability distribution for the difference in the azimuth of S_{Hmax} between the two time periods. A credible interval for the change in S_{Hmax} can then be calculated and used to assess the likelihood of a change in stress direction having taken place. Such intervals can similarly be used to determine thresholds for the detection of significant temporal changes in stress (Figure 14).

RESULTS

Clustering

We present results for three clustering schemes: k_{max} = 30 clusters for two-and three-dimensional clustering of all earthquakes in the dataset; and k_{rot} = 14 clusters for two-dimensional clustering of only those earthquakes shallower than 25 km. Maps of these three clustering schemes are shown in Figures 4-6, and the corresponding stress parameter estimates are listed in Tables 2-4.

The 2D and 3D clustering results for the data set as a whole (i.e. all 633 focal mechanisms) are broadly similar, as expected given the distribution of hypocenters and the moderate depth weighting used in the 3D case. In particular, we obtain in both cases 11 clusters in the vicinity of Mt Ruapehu and the King Country (insets in Figures 4 and 5), similar numbers of clusters in the southeast North Island and Marlborough, and three or four clusters in the northern TVZ and Raukumara Peninsula. The shallow 2D clustering (Figure 6) has a smaller number of clusters by design (that is, we have set the number of clusters to be 14, rather than 30 in the other two cases).

Stress estimates

The principal stress orientations computed with the 2D and 3D clustering are similar (Figures 8-10), and we confine our analysis in the first instance to the 2D clustering case (Figures 8). Several distinct stress domains are visible, which we can delineate on the basis of which principal stress is nearest vertical (S_1 vertical — normal stress regime; S_2 vertical — strike-slip; S_3 vertical — reverse stress regime). As anticipated based on surface faulting patterns, we obtain oblique reverse-faulting stress states for the Raukumara Peninsula and Marlborough. We obtain either normal or strike-slip stress states in other parts of the east coast and in the central North Island.

Once the estimated stress parameters have been converted to S_{Hmax} orientations using the Lund and Townend (2007) algorithm (Figures 11-13), the similarities between the two suites of results based on all earthquakes less than 50 km deep are clearer and several consistent patterns can be identified (cluster numbers refer to the 2D clustering case; Figure 11):

- NE–SW S_{Hmax} in the northern Taupo Volcanic Zone (cluster 3), a result consistent with that obtained for the Matata area by Hurst et al. (2008);
- ENE–WSW S_{Hmax} beneath the central and southern part of Lake Taupo; (cluster 24)
- ESE–WNW S_{Hmax} immediately southeast of Mt Ruapehu (cluster 26) and northwest of Mt Ruapehu (clusters 11, 12, 28);
- ENE–WSW S_{Hmax} between Mt Taranaki and Mt Ruapehu (clusters 1, 5, 10, 18, 23), with an anticlockwise rotation of approximately 20° near Waiouru (cluster 2) — the first of these two orientations is very similar to that obtained by Sherburn and White (2006) and Reyners (2009) along the Taranaki-Ruapehu line using crustal earthquakes, and the more northerly azimuth corresponds well to the orientation determined by Hayes et al. (2004) for a swarm of earthquakes near Waiouru;
- Uniform ENE–WSW S_{Hmax} from Hawke Bay to the Wanganui Basin (clusters 16, 17, 20, 27);

- S_{Hmax} subparallel to the east coast of the North Island south of Hawke Bay (clusters 8, 14, 19, 22);
- NE–SW S_{Hmax} in Cook Strait (clusters 7, 13);
- E–W S_{Hmax} in eastern Marlborough (clusters 4, 15, 21, 25), a result very similar to those of Balfour et al. (2005).

Where comparisons can be made between these new stress estimates and previous results (e.g. Balfour et al., 2005; Hayes et al., 2004; Sherburn and White, 2006, Hurst et al., 2008; Reyners, 2009), the measurements appear to be highly consistent.

The pattern of stress in the central North Island is particularly striking. Adjacent clusters typically exhibit highly similar S_{Hmax} orientations, suggesting that where pronounced differences do occur (e.g. in the vicinity of Mt Tongariro and southern Lake Taupo) these reflect real seismotectonic differences and not computational artefacts. The consistent ENE–WSW orientation observed at four locations between Mt Taranaki and Mt Ruapehu is clearly different from the orientation observed slightly further north. Detailed inspection of the focal mechanisms in clusters 11, 12, 26, and 28, which each exhibit a well-defined ESE–WNW S_{Hmax} orientation, reveals that while some of the mechanisms in cluster 11 are not very well determined, those in clusters 12, 26, and 28 are no less well determined than in adjacent clusters.

Using repeated earthquakes occurring near Waiouru, Johnson et al. (2007) obtained average orientations for the fast shear-wave propagation direction of ENE–WSW for stations within 10 km east and west of the Mt Ruapehu summit and NW–SE beneath Mt Ngauruhoe. These orientations and their spatial distribution are similar to what the S_{Hmax} results reveal, suggesting that the two modal stress directions observed in the vicinity of Mt Ruapehu are both real. We have not yet compared the two data sets in detail, but this preliminary comparison suggests that a comprehensive analysis of stress and seismic anisotropy in the vicinity of Mt Ruapehu (cf. Gerst and Savage, 2004) will provide important insight into what factors control these parameters.

Comparison of the stress results obtained for the 2D and 3D clustering enables some comments to be made regarding vertical variations in stress. As noted above, the two suites of results are generally similar, but some differences are apparent, particularly in the southern North Island and Marlborough. The 3D cluster 13 exhibits an S_{Hmax} orientation approximately orthogonal to the adjacent clusters and to the NE–SW orientation seen for the 2D clustering. The centroid depth for 3D cluster 13 is 10 km, whereas those of the adjacent clusters 3 and 27 are 46 km and 29 km, respectively. Similarly, 3D clusters 29 and 30 have centroid depths of 34 and 11 km, respectively, with the shallower measurement matching well the WNW–ESE orientation computed by Balfour et al. (2005). In other words, the S_{Hmax} orientations that appear discrepant in map view actually represent stress estimates at different depths.

It is interesting to note that, in contrast, variations in depth do not appear to account for the different S_{Hmax} orientations observed in both the 2D and 3D clustering cases for central Hawkes Bay (2D clusters 19 and 20; 3D clusters 14 and 24). In both cases, the northern S_{Hmax} orientation is rotated clockwise by 30–40° with respect to the southern orientation, but all four clusters have centroid depths greater than 30 km. A more detailed local study of the focal mechanisms and stress in this area may clarify whether these local variations in stress are related to the boundary between locked (southern) and slipping (northern) sections of the subduction thrust proposed on the basis of geodetic fault slip inversions (Wallace et al., 2004).

As noted above, we have performed a third clustering of the focal mechanism data set using only those earthquakes shallower than 25 km (Figure 6). This provides an upper- to mid-crustal view of the prevailing stressses and some differences from the 50 km 2D and 3D results are apparent. Once again, the results exhibit close agreement between adjacent clusters except in the vicinity of Mt Ruapehu, where two dominant S_{Hmax} orientations are observed. The similarity of 25 and 50 km results in the TVZ is not surprising given that the seismogenic zone there is significantly thinner than 25 km (Bryan et al., 1999). Stress orientations in the southern North Island and Marlborough are found to be uniformly WNW–ESE, as previously reported by Balfour et al. (2005), and a consistent NE–SW orientation in the Wanganui Basin is also evident.

The algorithm used to compute stress parameters here is a recent development and has not yet been widely applied (Arnold and Townend, 2007; Mazzotti and Townend, submitted), and it is useful to compare the results with those obtained using an alternative algorithm. Figure 15 illustrates a comparison of the S_{Hmax} results obtained for all three suites of focal mechanism clusters using the Arnold and Townend (2007) Bayesian stress estimation algorithm and the commonly employed Michael algorithm (Michael, 1984, 1987). The two algorithms give very similar estimates of the mean S_{Hmax} direction in each case.

One advantage of the Arnold and Townend (2007) algorithm over other stress estimation codes (cf. Michael, 1984, 1987; Gephart and Forsyth, 1997; Robinson and McGinty, 2000; Abers and Gephart, 2001) is the facility to include various weighting factors in the estimation formulation. All such inversion methods (Arnold and Townend 2007 included) make the assumption that the focal mechanisms included in an inversion all arise from a region with a single stress field. However the most distant focal mechanisms in a cluster are likely to be affected by a stress field that differs from that close to the cluster centroid. Rather than restrict analysis only to the most spatially compact clusters (with a corresponding reduction in sample size and precision), we instead include but down-weight the more distant focal mechanisms. Figure 16 shows the effects of altering the distance-weighting threshold referred to in the previous section for five of the 2D clusters. There is clearly no significant change in the mean S_{Hmax} direction computed for distance thresholds (beyond which a focal mechanism does not contribute to the stress estimate) of 0–50 km. This suggests that the stress estimates reported here are unlikely to be unduly biased by the incorporation of focal mechanisms lying at reasonable distances from each cluster centroid.

Temporal stress changes

We have selected five clusters from the 2D clustering for analysis of temporal changes, three in the southern TVZ close to Mt Ruapehu (clusters 2, 10, 28) and two control clusters, one in the Matata area in the Bay of Plenty (cluster 3), a recent site of ongoing earthquake swarm activity and one in southern Hawkes Bay (cluster 22). For each cluster we divide the sequence of earthquakes into an early and a late part. This is done by inspecting the histogram of earthquake times, and visually identifying a natural break point (an interval with no earthquakes), or by simply dividing at the midpoint of the time interval if no natural break was visible.

Figure 14 shows the results for cluster 10 (due west of Ruapehu). This cluster was split into early and late portions at the midpoint of the time interval, as indicated by the vertical dashed red line on the histogram. Separate stress estimates for the two time periods lead to the two stereonets in the lower left of Figure 14: these diagrams suggest a clockwise rotation of the stress field. The posterior probability distributions for the direction of S_{Hmax} in the two epochs are shown at the right: the modes of the early ('1') and late ('2') distributions are clearly at different locations (approximately 040°E and 075°E degrees respectively). We assess the statistical significance of this difference by deriving the probability distribution for the difference in S_{Hmax} direction, which is shown at lower right, together with a 95% Bayesian credible interval (indicated by vertical dashed lines). The point estimate of the difference (early-late) is -35°, with a 95% interval estimate of (-60°,-9°). This interval estimate excludes 0° and is evidence that the S_{Hmax} direction differs between the two time periods.

We have repeated analyses such as that described above for the other four clusters, and show the results in Table 5. For each cluster we give point and interval estimates for the S_{Hmax} direction for the whole dataset, and for the early and late sequences separately. We also give an estimate of the change in S_{Hmax} direction with a 95% credible interval, which can be used to test for significant changes. In this table we also quote the margins of error (MOE), or half widths of the credible intervals for $\Delta S_{Hmax.}$ These margins of error are all of the order of 30°, which is the typical minimum size of stress rotation that we are able to detect using this method, for clusters of around 20 focal mechanisms.

Inspecting the credible intervals in Table 5 we find that in addition to the change found for cluster 10, a significant change in stress direction is also indicated for cluster 3 (Bay of Plenty) where $\Delta S_{Hmax} = -50°$ (95% CI: (-88°,-11°)). However some caution must be exercised in the interpretation of this result: we have plotted the depths and times of the focal mechanisms in these two clusters in Figure 17, and there is an apparent change in the typical depth of the earthquakes in the early and late parts of cluster 3. This represents a change in earthquake location from within the network to the network boundary, where depths are less well-constrained and tend to be fixed at 5 km, so that the detection of a change in stress may be spatial rather than temporal. No such systematic change in depth is apparent in cluster 10, so that the observed rotation of the S_{Hmax} direction does appear in this case to represent a genuine temporal change.

DISCUSSION AND CONCLUSIONS

Clustering

Although a wide range of clustering parameters are possible, our results suggest that the actual clusters used in the stress analysis are fairly insensitive to the exact clustering parameters employed. Despite this observation, any future studies repeating this or similar analysis using different focal mechanism data sets would inevitably obtain different clustering results, making a direct comparison of stress measurements difficult. In particular, in order to look for temporal stress changes, we should ideally use the same clusters from epoch to epoch. One solution would be to define the clusters used in subsequent studies on the basis of the focal mechanism data set and corresponding clustering employed here. This seems an unsatisfactory approach however, since the data set used here represents a snap-shot of seismicity that is unlikely to adequately define long-term patterns of earthquake clustering.

A better solution may be to define clusters using the long-term earthquake distribution, which is less likely to change, and then to allocate future focal mechanisms to those clusters. This would enable different studies to compute stress parameters — or other parameters such as strain rates — at a common set of locations. One benefit of this approach is that all well-located earthquakes can be used to define the clustering; in other words, we are not restricted to only those earthquakes with sufficient first motion parameters for focal mechanisms to be computed.

We have made a preliminary attempt at clustering the long-term seismicity by applying the K-means algorithm to 20 years' data (Figure 18). We have extracted approximately 26,000 earthquakes larger than magnitude 3 occurring between 1 January 1989 and 1 January 2009, and allocated them to $k_{rot} = 114$ clusters. This results in a much coarser clustering in areas of particular interest (such as the southern TVZ) than we have analyzed in the current study, but may be a reasonable way of tackling the problem of long-term stress monitoring in future studies.

Stress orientations

We have assembled the largest collection of focal mechanisms and horizontal stress orientations in New Zealand. Our S_{Hmax} estimates are generally consistent with previously published results from Marlborough, the TVZ and Taranaki.

West of Ruapehu, we observe S_{Hmax} orientations of ESE-WNW, contrasting with ENE-WSW in the adjacent TVZ and Taranaki-Ruapehu Line. While we need to examine these data in more detail, our preliminary work suggests these orientations are real. We also observe apparent depth dependent S_{Hmax} orientations.

Detection of temporal changes in stress orientation

We have demonstrated the feasibility of detecting spatiotemporal variations in stress (specifically changes in the S_{Hmax} direction). We have shown that we are able to detect geophysically significant changes (S_{Hmax} rotations greater than approximately 30°) with datasets of practicable size (20 or more focal mechanisms). Interpretation of changes as spatial or temporal needs to rely on reliable clustering of focal mechanisms and we need to take into account time dependent changes in the locations.

Future work

For this study, we calculated focal mechanisms with the widely used program FPFIT (Reasenberg and Oppenheimer, 1985). As mechanisms determined this way have several uncertainty measures (error in dip, strike and rake of focal planes, number of first motion misfits, and their distribution statistic), it is not always clear which measures we should use to ensure that mechanisms are suitable for stress determination. Roman et al. (2004) and Roman et al. (2006) required focal mechanisms to satisfy all of the above criteria, with additionally requiring that the maximum uncertainty in P- and T-axes be less than 25% of the focal sphere. With our data processing method, we could easily place limits on the focal plane orientation uncertainties, first motion misfits, and the first motion distribution statistic, but it is not clear what bounds are appropriate.

We have also observed that there can be many up and few down first motions (or vice versa), in which case the mechanism will be poorly determined. This consideration is not part of the FPFIT output information, though we could easily pre-screen and eliminate these events.

One way to bypass the need to select focal mechanisms using multiple adhoc FPFIT uncertainty parameters is to use a new probabilistic (Bayesian) method (Walsh et al., 2008) to determine focal mechanisms. We could then determine whether or not to use a particular mechanism based on a single value, namely the scalar concentration parameter, *κ,* which is inversely related to the standard deviation of focal mechanism parameters. The method of Walsh et al. (2008) uses the probabilistic representation of a hypocentre recalculated from *GeoNet* data. We would probably use the *GeoNet* non-probabilistic hypocentre which would require some modification to the existing algorithm.

As our goal in this project has been to develop a benchmark against which to look for temporal stress changes in the southern TVZ, we only considered earthquakes less than 50 km deep. Despite this limitation, we have compiled the largest sample of stress data yet assembled in New Zealand. We therefore intend to expand our analysis to deeper earthquakes to try to obtain the full picture of stress beneath New Zealand, including stresses associated with the two subduction zones.

Once we have implemented the Bayesian method of determining focal mechanisms on data from all depths, we will write a paper on our results. At this stage our primary goal will be to describe the *state of stress* beneath New Zealand, with a secondary goal looking at potential stress change and the spatiotemporal benchmark that formed the goal of this study. We anticipate that the results of this more extensive study to be suitable for publication in EPSL or JGR.

REFERENCES

Abers, G.A., Gephart, J.W., 2001, Direct inversion of earthquake first motions for both the stress tensor and focal mechanisms and application to southern California, *Journal of Geophysical Research*, 106: 26523-26540.

Arnold, R., and Townend, J., 2007, A Bayesian approach to estimating tectonic stress from seismological data: *Geophysical Journal International*, 170: 1336-1356.

Balfour, N.J., Savage, M.K., and Townend, J., 2005, Stress and crustal anisotropy in Marlborough, New Zealand: Evidence for low fault strength and structure-controlled anisotropy: *Geophysical Journal International*, 163: 1073-1086.

Bryan, C.J., Sherburn, S., Bibby, H.M., Bannister, S.C., Hurst, A.W., 1999, Shallow seismicity of the central Taupo Volcanic Zone, New Zealand: its distribution and nature. *New Zealand Journal of Geology and Geophysics*, 42: 533 – 542.

Bryan, C.J., and Sherburn, S., 1999, Seismicity associated with the 1995-1996 eruptions of Ruapehu volcano, New Zealand: Narrative and insights into physical processes: *Journal of Volcanology and Geothermal Research*, 90: 1-18.

Gephart, J.W., Forsyth, D., 1984, An improved method for determining the regional stress tensor using earthquake focal mechanism data: application to the San Fernando earthquake sequence. *Journal of Geophysical Research*, 89: 9305-9320.

Gerst, A., and Savage, M.K., 2004, Seismic anisotropy beneath Ruapehu Volcano: A possible eruption forecasting tool: *Science*, 306: 1543-1547.

Hartigan, J.A., 1975, Clustering Algorithms: Hoboken, N.J., John Wiley, 351 p.

Hayes, G., Reyners, M., and Stuart, G., 2004, The Waiouru, New Zealand, earthquake swarm: Persistent mid crustal activity near an active volcano: *Geophysical Research Letters*, 31: L19613 1-4.

Hurst, A.W., and McGinty, P.J., 1999, Earthquake swarms to the west of Mt Ruapehu preceding its 1995 eruption: *Journal of Volcanology and Geothermal Research*, 90: 19-28.

Hurst, T., Bannister, S., Robinson, R., and Scott, B., 2008, Characteristics of three recent earthquake sequences in the Taupo Volcanic Zone, New Zealand: *Tectonophysics*, 452: 17-28.

Johnson, J., Wessel, A., Savage, M.K., and Hurst, T., 2007. Seismic anisotropy as an eruption forecasting tool at Mount Ruapehu. Geosciences '07 conference, Tauranga, Geological Society of New Zealand Miscellaneous Publication 123A.

Lund, B., and Townend, J., 2007, Calculating horizontal stress orientations with full or partial knowledge of the tectonic stress tensor: *Geophysical Journal International*, 170: 1328-1335.

Mardia, K.V., Kent, J.T., and Bibby, J.M., 1979, Multivariate analysis: London, 521 p.

Mazzotti, S., and Townend, J., 2009. State of stress in central and eastern North America seismic zones. *Lithosphere*, submitted (June 2009).

McKenzie, D.P., 1969, Relation between fault plane solutions for earthquakes and the directions of the principal stresses: *Bulletin of the Seismological Society of America*, 59: 591-601.

Michael, A.J., 1984, Determination of stress from slip data: faults and folds: *Journal of Geophysical Research*, 89: 11517-11526.

—, 1987, Use of focal mechanisms to determine stress: a control study: *Journal of Geophysical Research*, 92: 357-368.

Miller, V., and Savage, M., 2001, Changes in seismic anisotropy after volcanic eruptions: Evidence from Mount Ruapehu: *Science*, 293: 2231-2233.

Reasenberg, P.A., and Oppenheimer, D., 1985, FPFIT, FPPLOT and FPPAGE: Fortran computer programs for calculating and displaying earthquake fault-plane solutions: *U.S. Geol. Surv. Open-File Rept. 85-739*: 109.

Reyners, M., 2009, Stress and strain from earthquakes at the southern termination of the Taupo Volcanic Zone, New Zealand: *Journal of Volcanology and Geothermal Research.*

Ristau, J., 2008, Implementation of routine regional moment tensor analysis in New Zealand: *Seismological Research Letters*, 79: 400-415.

Robinson, R., McGinty, P.J., 2000, The enigma of the Arthur's Pass, New Zealand, earthquake 2. The aftershock distribution and its relation to regional and induced stress fields: *Journal of Geophysical Research*, 105: 16139-16150.

Roman, D.C., Moran, S.C., Power, J.A., and Cashman, K.V., 2004, Temporal and spatial variation of local stress fields before and after the 1992 eruptions of Crater Peak vent, Mount Spurr volcano, Alaska: *Bulletin of the Seismological Society of America*, 94: 2366-2379.

Roman, D.C., Neuberg, J., and Luckett, R.R., 2006, Assessing the likelihood of volcanic eruption through analysis of volcanotectonic earthquake fault-plane solutions: *Earth and Planetary Science Letters*, 248: 229-237.

Sherburn, S., Bryan, C.J., Hurst, A.W., Latter, J.H., and Scott, B.J., 1999, Seismicity of Ruapehu volcano, New Zealand, 1971-1996: A review. *Journal of Volcanology and Geothermal Research*, 88: 255-278.

Sherburn, S., White R.S., 2006 Tectonics of the Taranaki region, New Zealand: earthquake focal mechanisms and stress axes. *New Zealand Journal of Geology and Geophysics*, 49: 269 – 279.

Townend, J., 2006, What do faults feel? Observational constraints on the stress acting on seismogenic faults: *Earthquakes: Radiated Energy and Physics of Faulting*, 170: 313-327.

Townend, J., and Zoback, M.D., 2001, Implications of earthquake focal mechanisms for the frictional strength of the San Andreas fault system, Geological Society Special Publication, p. 13-21.

—, 2004, Regional tectonic stress near the San Andreas fault in central and southern California: *Geophysical Research Letters*, 31: L15S11 1-5

—, 2006, Stress, strain, and mountain building in central Japan: *Journal of Geophysical Research B: Solid Earth*, 111, B03411, doi:10.1029/2005JB003759.

Wallace, L.M., Beavan, J., McCaffrey, R., Darby, D., 2004, Subduction zone coupling and tectonic block rotations in the North Island, New Zealand. *Journal of Geophysical Research B: Solid Earth*, 109: B12406.

Walsh, D., Arnold, R., Townend, J., 2008, A Bayesian approach to determining and parametrizing earthquake focal mechanisms. *Geophysical Journal International* doi:10.111/j.1365-246X.2008.03979.x.

Wessel, P., and Smith, W.H.F., 1991, Free software helps map and display data: *Eos*, 72: 441,445-446.

FIGURES

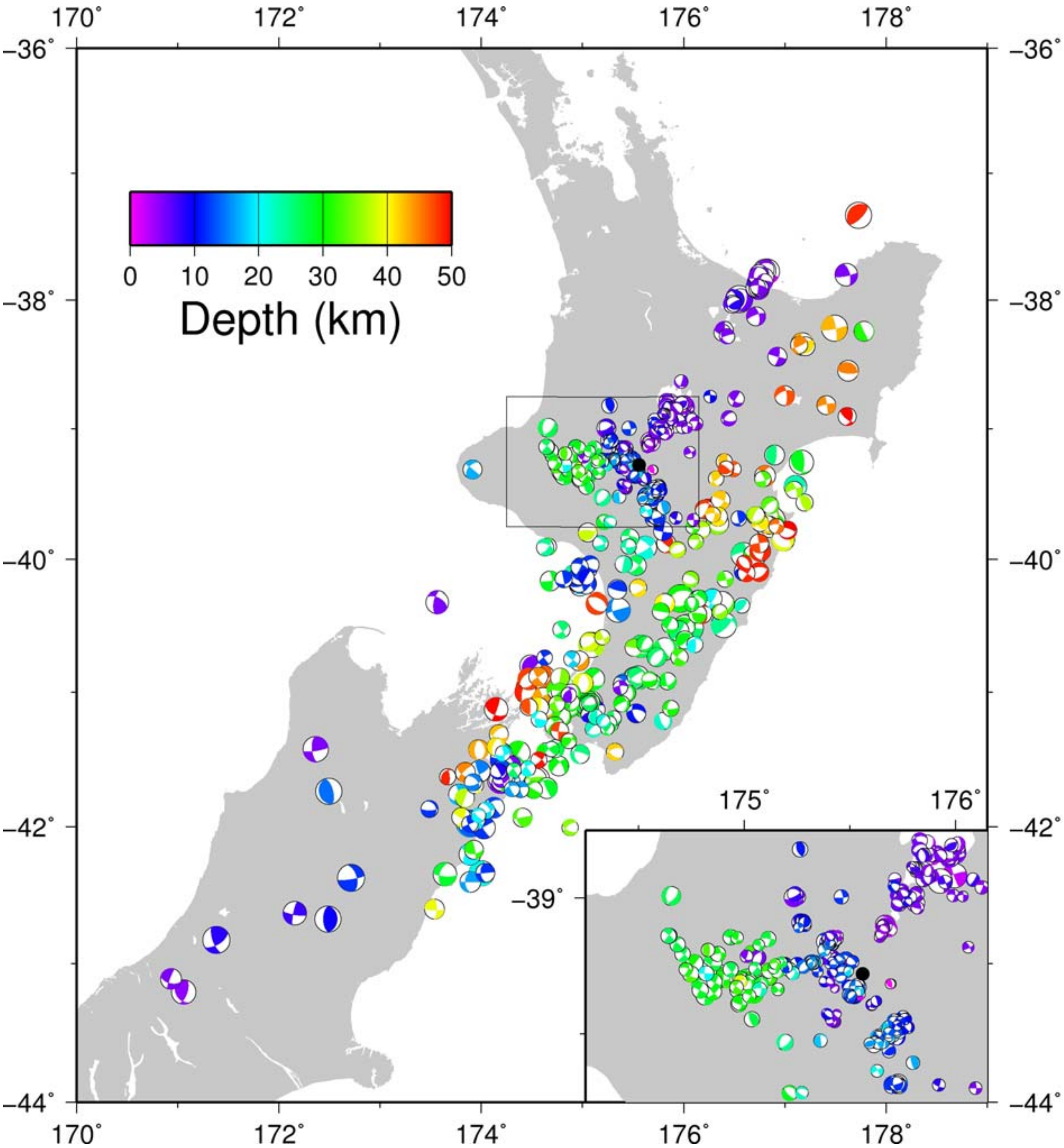

Figure 1 Locations and focal mechanisms for 633 earthquakes from the *GeoNet* database used in this study. The earthquake search parameters are shown in Table 1. The southern TVZ area is illustrated at larger scale in the bottom right of the map. Mt Ruapehu is marked by a black circle. Any focal mechanisms plotting outside the map are not shown.

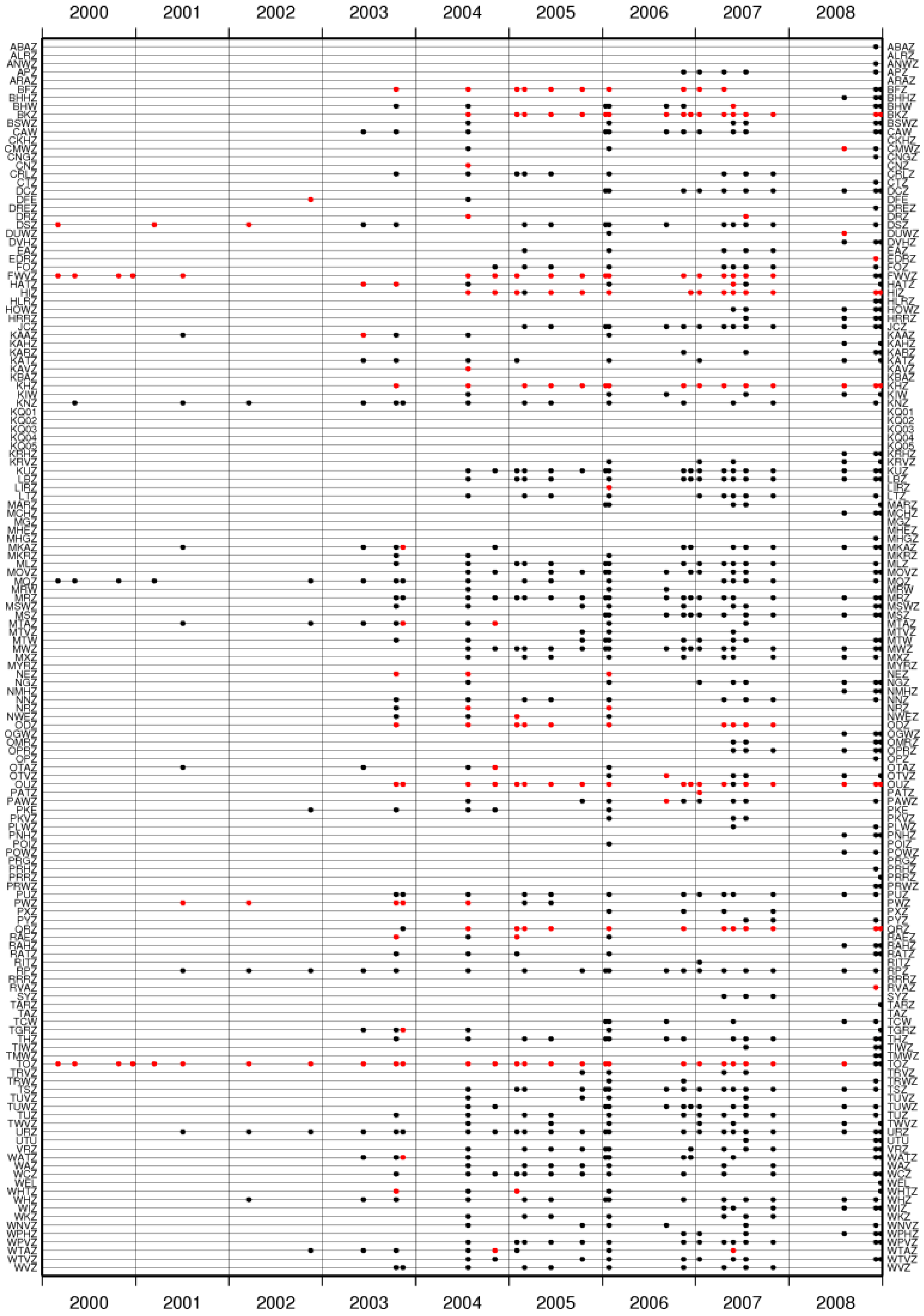

Figure 2 Summary of polarity errors observed at New Zealand seismographs for 2000 to 2008. A black symbol indicates a correct polarity and a red symbol a reversed polarity (a polarity error). Seismograph sites codes are shown on the right and left of the figure.

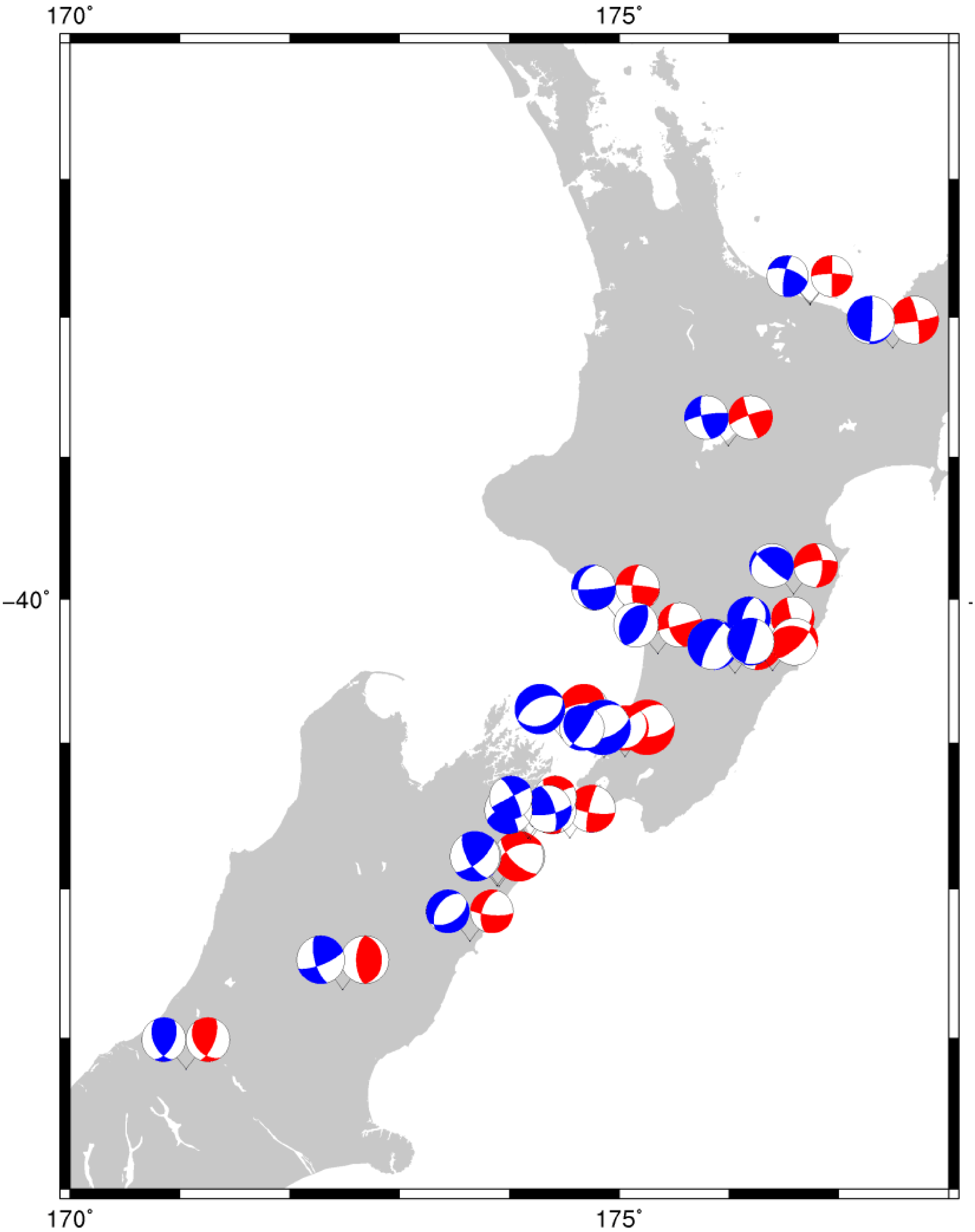

Figure 3 Comparison of focal mechanisms from this study (red) with moment tensor solutions of Ristau (2008) (blue).

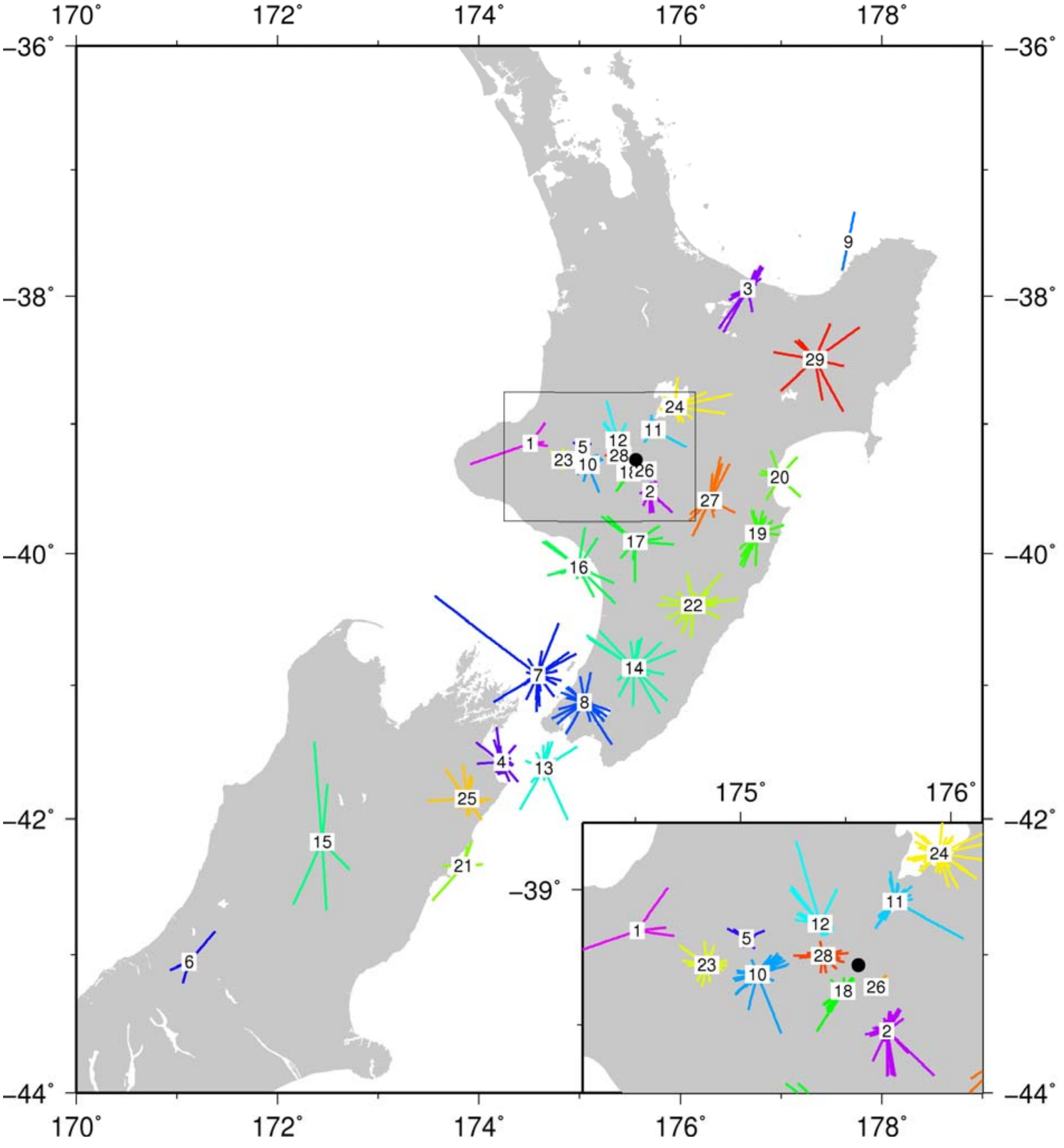

Figure 4 Clustering results for the two-dimensional case using k_{max} = 30, which gives an average of 20 focal mechanisms per cluster. A line links each focal mechanism to its respective cluster centroid (i.e. the mean position for that cluster). The number at the centroid of each cluster is the cluster number. The southern TVZ area is illustrated at larger scale in the bottom right of the map. Mt Ruapehu is marked by a black circle.

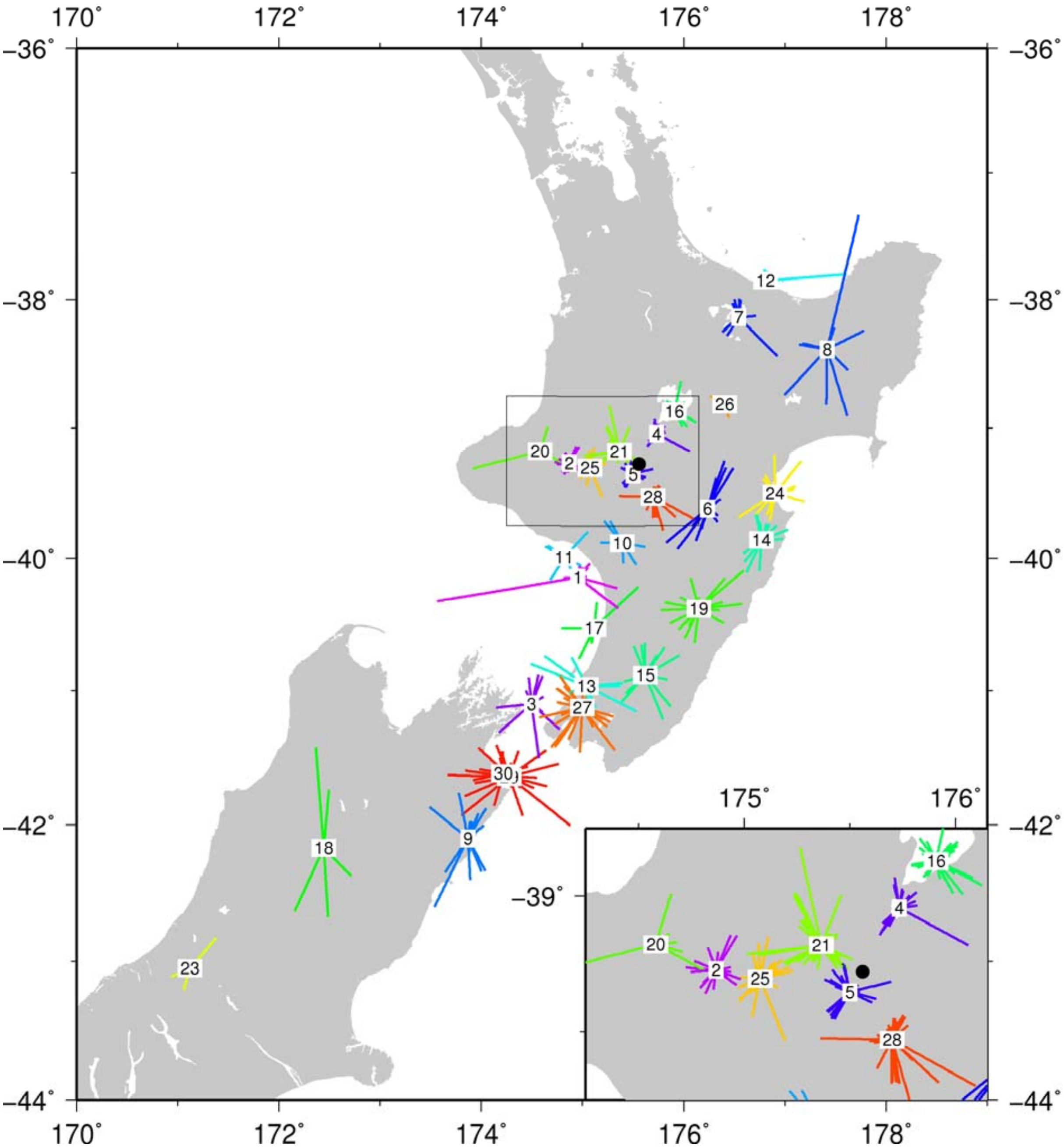

Figure 5 Clustering results for the three-dimensional case using $k_{max} = 30$, which gives an average of 20 focal mechanisms per cluster, and a depth-weighting factor of 3. A line links each focal mechanism to its respective cluster centroid (i.e. the mean position for that cluster). The number at the centroid of each cluster is the cluster number. The southern TVZ area is illustrated at larger scale in the bottom right of the map. Mt Ruapehu is marked by a black circle.

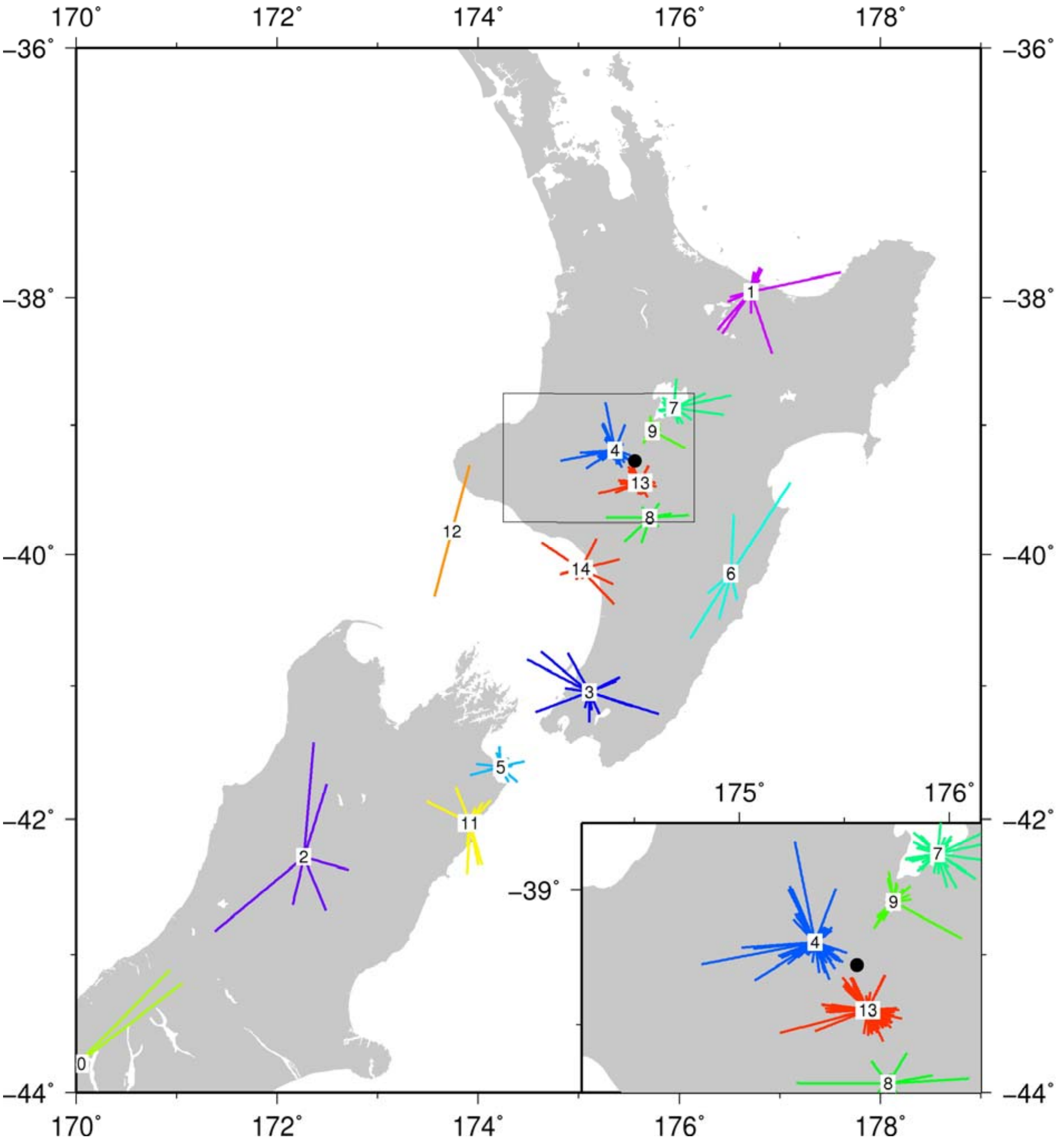

Figure 6 Two-dimensional clustering results for earthquakes shallower than 25 km using k_{rot} = 14. A line links each focal mechanism to its respective cluster centroid (i.e. the mean position for that cluster). The number at the centroid of each cluster is the cluster number. The southern TVZ area is illustrated at larger scale in the bottom right of the map. Mt Ruapehu is marked by a black circle.

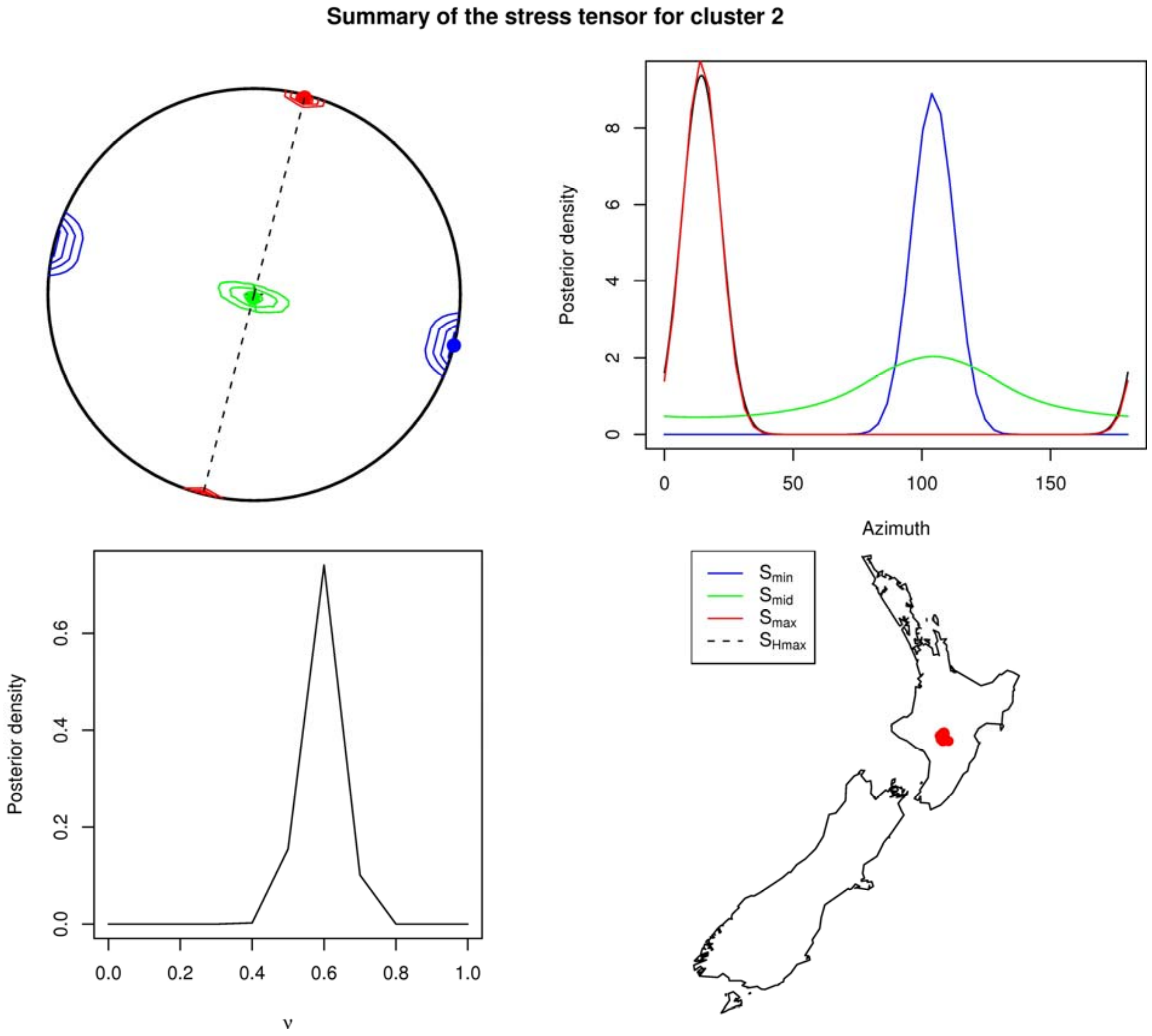

Figure 7 Figure showing an example of the output from the Bayesian stress estimation algorithm (Arnold and Townend, 2007) for cluster 02 in the 2D clustering. The top left diagram shows the posterior distributions of the three principal stress axes, in stereographic projection. The red, green, and blue contours represent S_1, S_2, and S_3, respectively, and the dashed line represents the corresponding S_{Hmax} azimuth. The top right diagram shows one-dimensional posterior distributions of the three principal stress axes' azimuths and the S_{Hmax} azimuth (black curve). In this particular case, the S_{Hmax} and S1 azimuths are parallel, since S_2 is almost exactly vertical (Lund and Townend, 2007). The lower left panel illustrates the posterior distribution of the stress ratio ($\nu = (S_1 - S_2)/(S_1 - S_3)$), and the lower right panel shows the geographic location of the cluster.

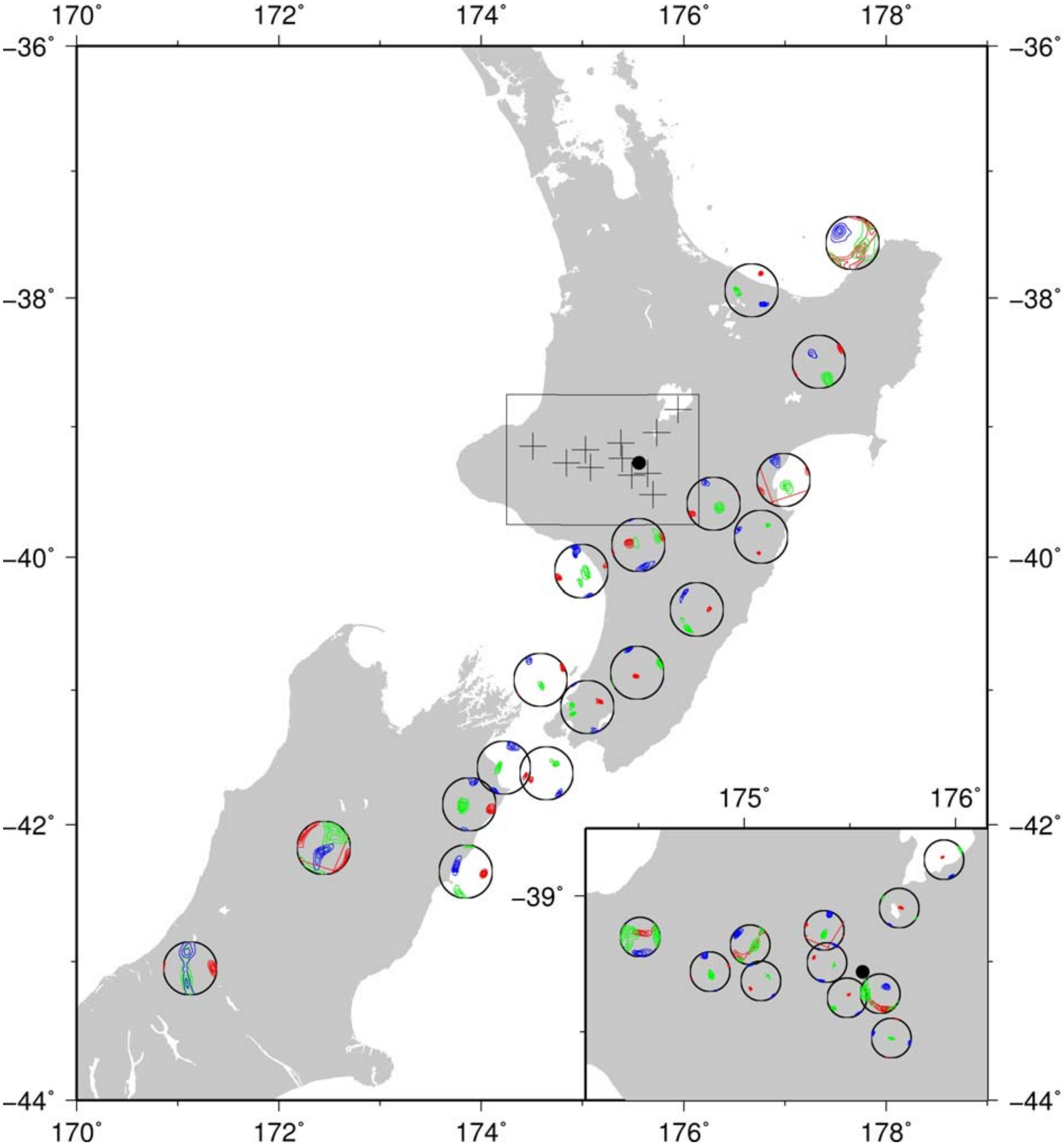

Figure 8 Stereonets showing the orientations of the three principal stresses computed for each cluster in the two-dimensional clustering case (Figure 4). S_1 is shown in red, S_2 in green, and S_3 in blue. The southern TVZ area is illustrated at larger scale in the bottom right of the map. Mt Ruapehu is marked by a black circle. Results corresponding to the southwesternmost cluster (cluster number 30), which plots outside the lower left corner of the map, have been removed for clarity.

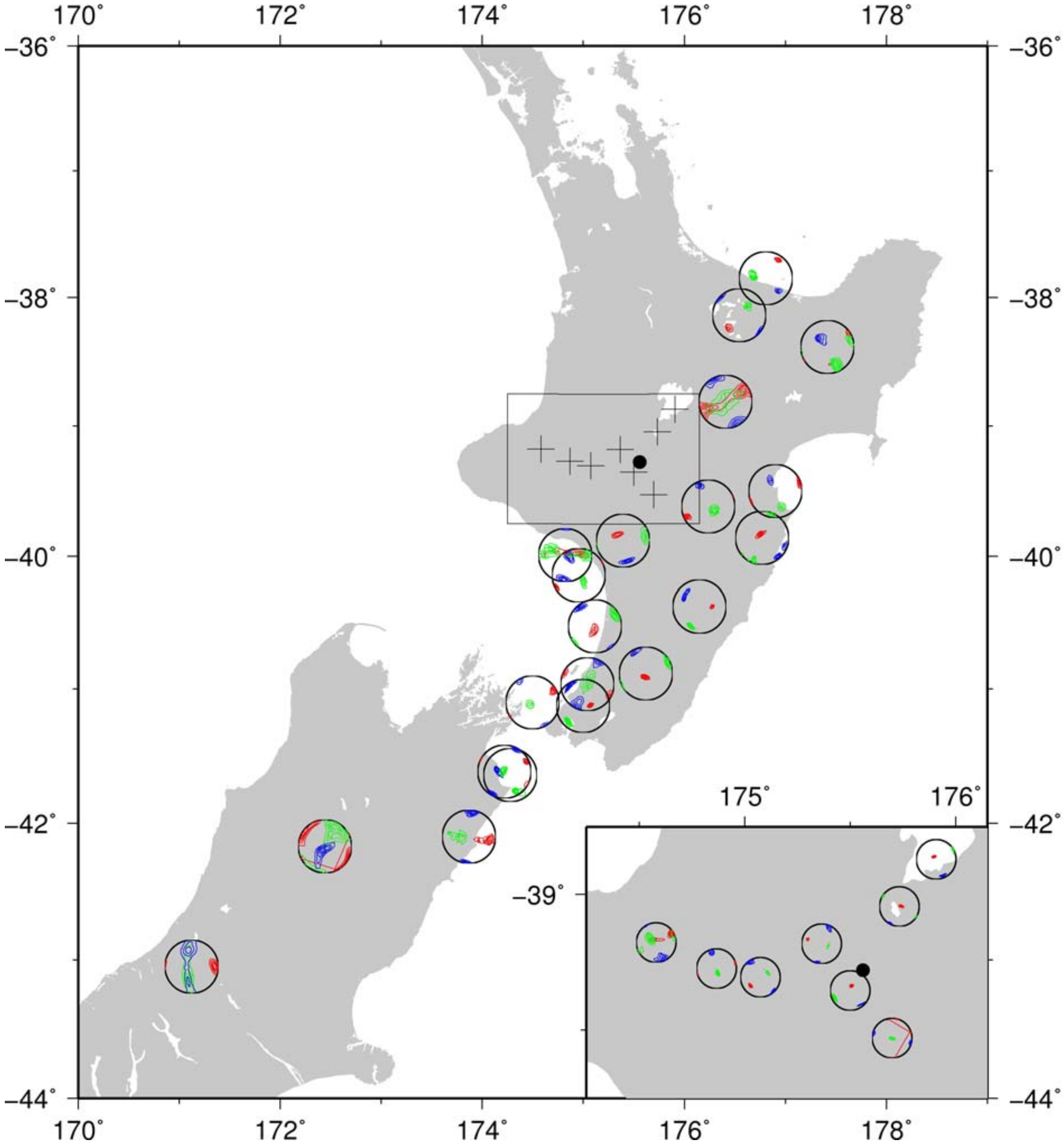

Figure 9 Stereonets showing the orientations of the three principal stresses computed for each cluster in the three-dimensional clustering case (Figure 5). S_1 is shown in red, S_2 in green, and S_3 in blue. The southern TVZ area is illustrated at larger scale in the bottom right of the map. Mt Ruapehu is marked by a black circle. Results corresponding to the southwesternmost cluster (cluster number 22), which plots outside the lower left corner of the map, have been removed for clarity.

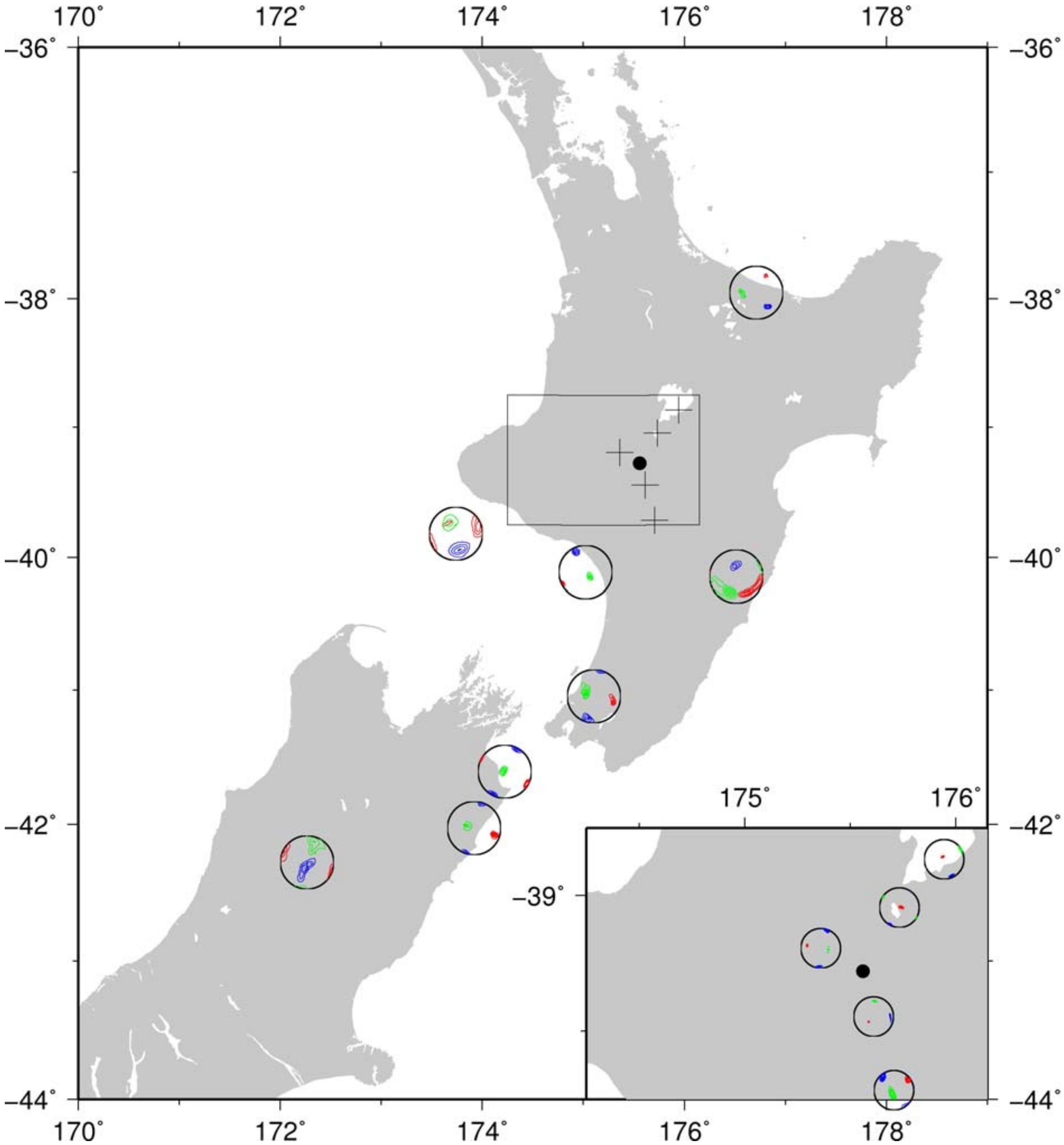

Figure 10 Stereonets showing the orientations of the three principal stresses computed for each cluster in the two-dimensional clustering of earthquakes shallower than 25 km (Figure 6). S_1 is shown in red, S_2 in green, and S_3 in blue. The southern TVZ area is illustrated at larger scale in the bottom right of the map. Mt Ruapehu is marked by a black circle. Results corresponding to the southwesternmost cluster (cluster number 10), which plots outside the lower left corner of the map, have been removed for clarity.

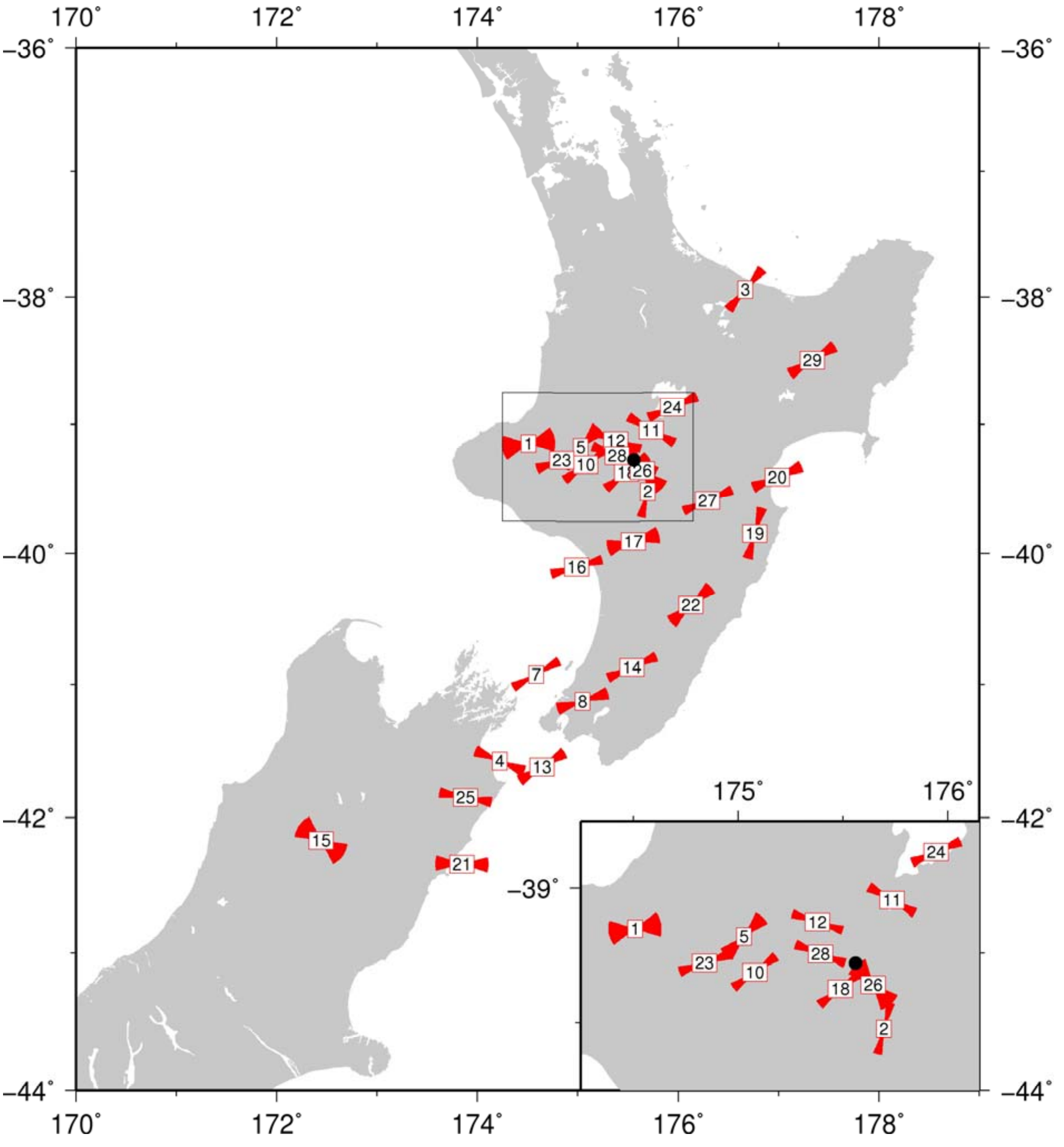

Figure 11 Map of estimated S_{Hmax} orientations (90% confidence intervals) for the two-dimensional clustering case (Figure 4 and Figure 8). The southern TVZ area is illustrated at larger scale in the bottom right of the map. Mt Ruapehu is marked by a black circle.

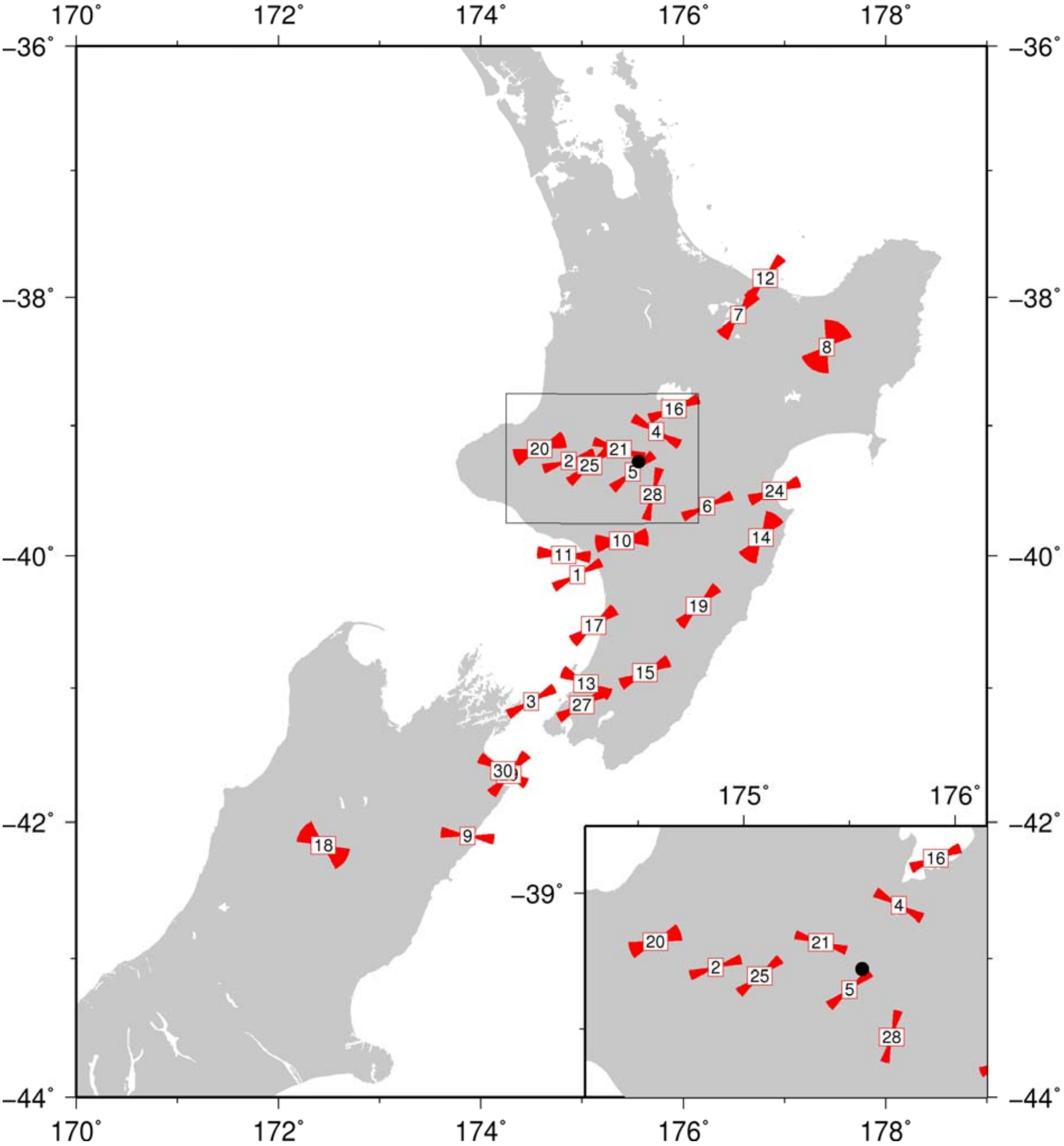

Figure 12 Map of estimated S_{Hmax} orientations (90% confidence intervals) for the three-dimensional clustering case (Figure 5 and Figure 9). The southern TVZ area is illustrated at larger scale in the bottom right of the map. Mt Ruapehu is marked by a black circle.

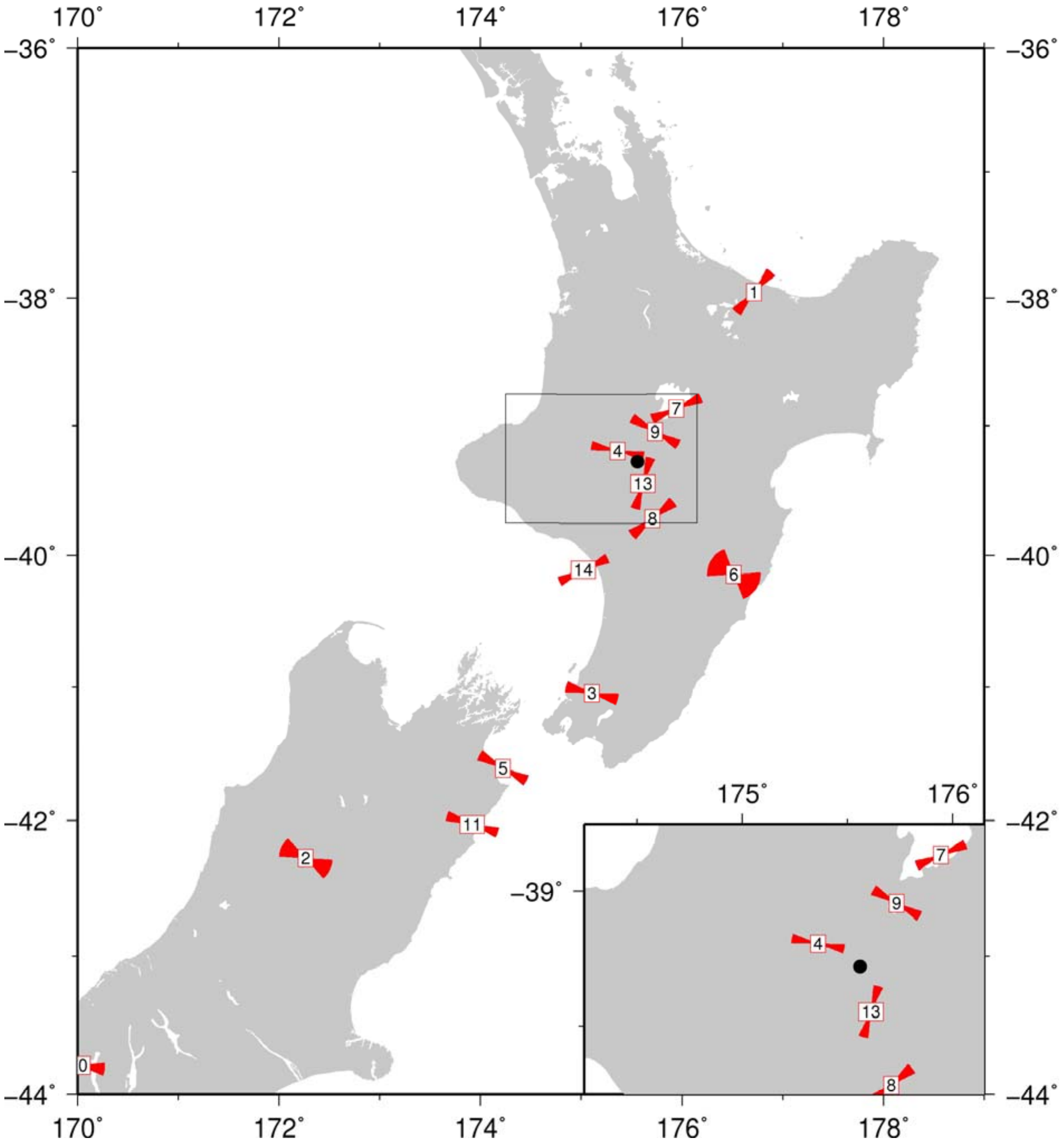

Figure 13 Map of estimated S_{Hmax} orientations (90% confidence intervals) for the two-dimensional clustering case of earthquakes shallower than 25 km (Figure 6 and Figure 10). The southern TVZ area is illustrated at larger scale in the bottom right of the map. Mt Ruapehu is marked by a black circle.

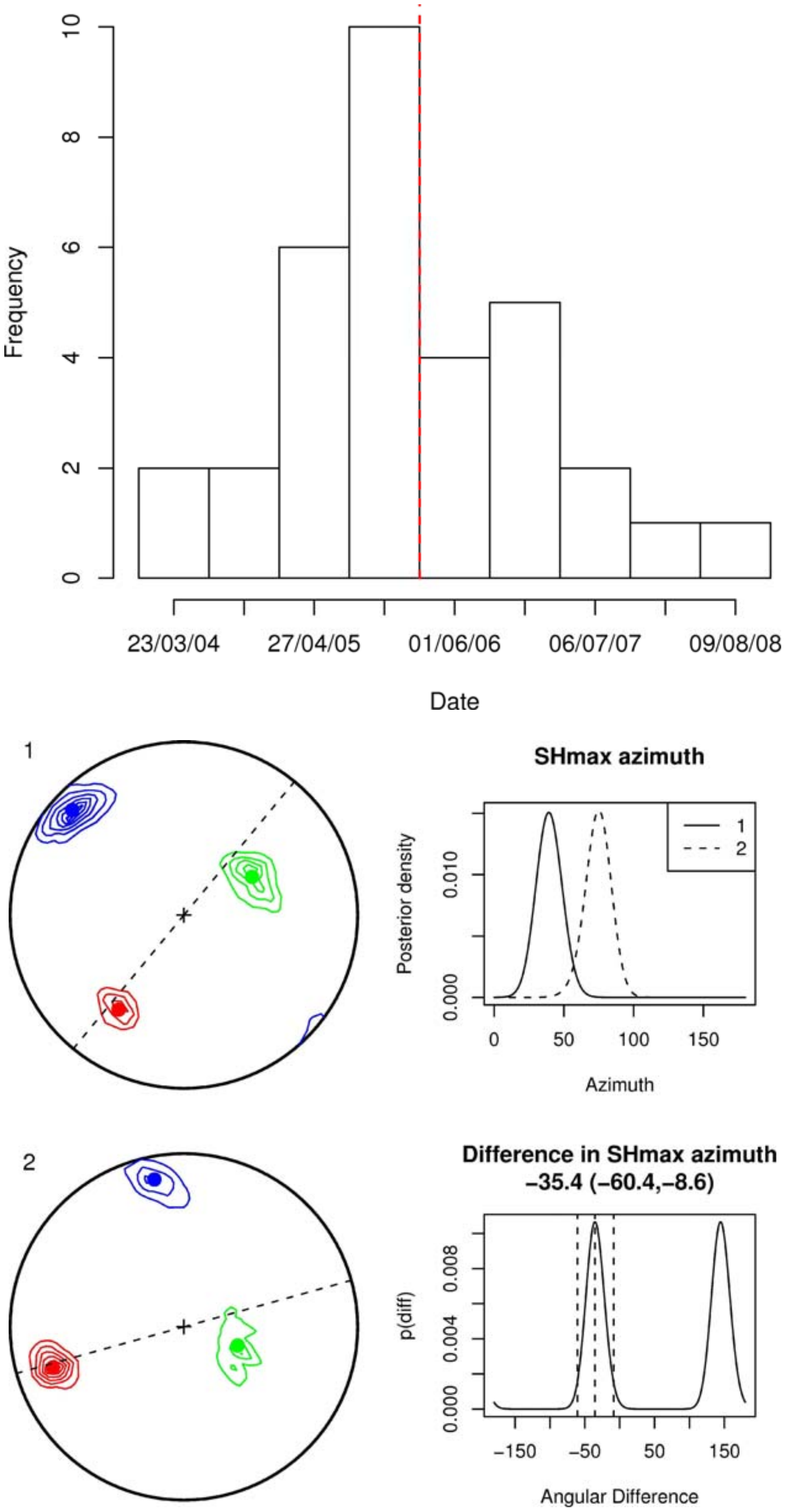

Figure 14 Example output for the temporal stress change analysis in the case of cluster 10 (2D clustering). The uppermost histogram illustrates the timing of the earthquakes in this cluster, with the dashed red line marking the point at which the cluster was partitioned. The lower four panels show the principal stress orientations computed for the earlier ("1") and later ("2") groups of focal mechanisms in stereographic project (left-hand panels) and posterior distributions of S_{Hmax} azimuth (right-hand panels). In this case, since the 95% credible interval for the difference (-60.4,-8.6) excludes zero, the two S_{Hmax} direction estimates are significantly different.

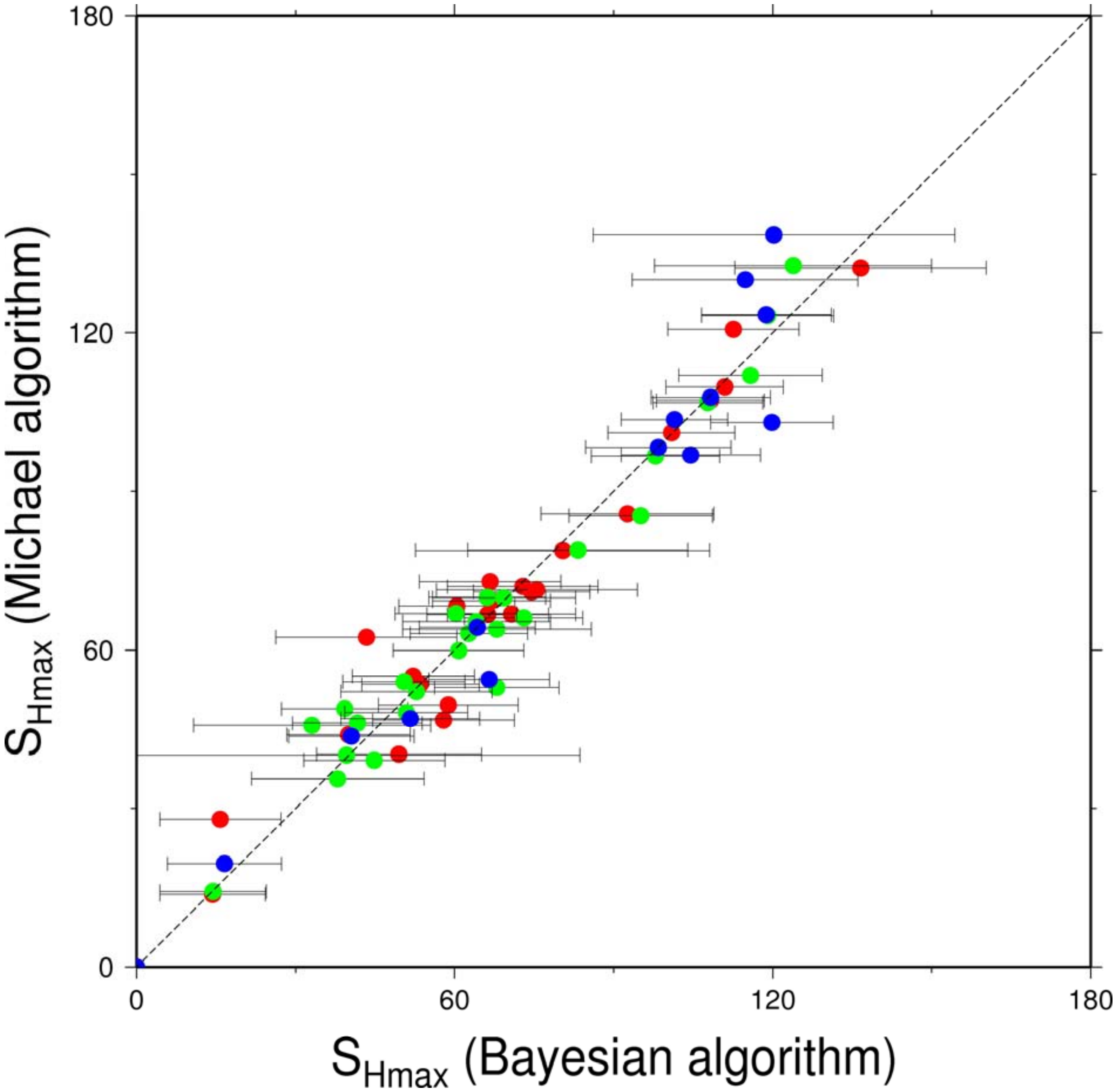

Figure 15 Comparison of the S_{Hmax} orientations obtained with the Bayesian algorithm (Arnold and Townend, 2007) and the commonly used alternative algorithm of Michael (1984, 1987). Symbols are coloured according to the clustering method 2D, 3D - 50 km, or 3D – 25 km.

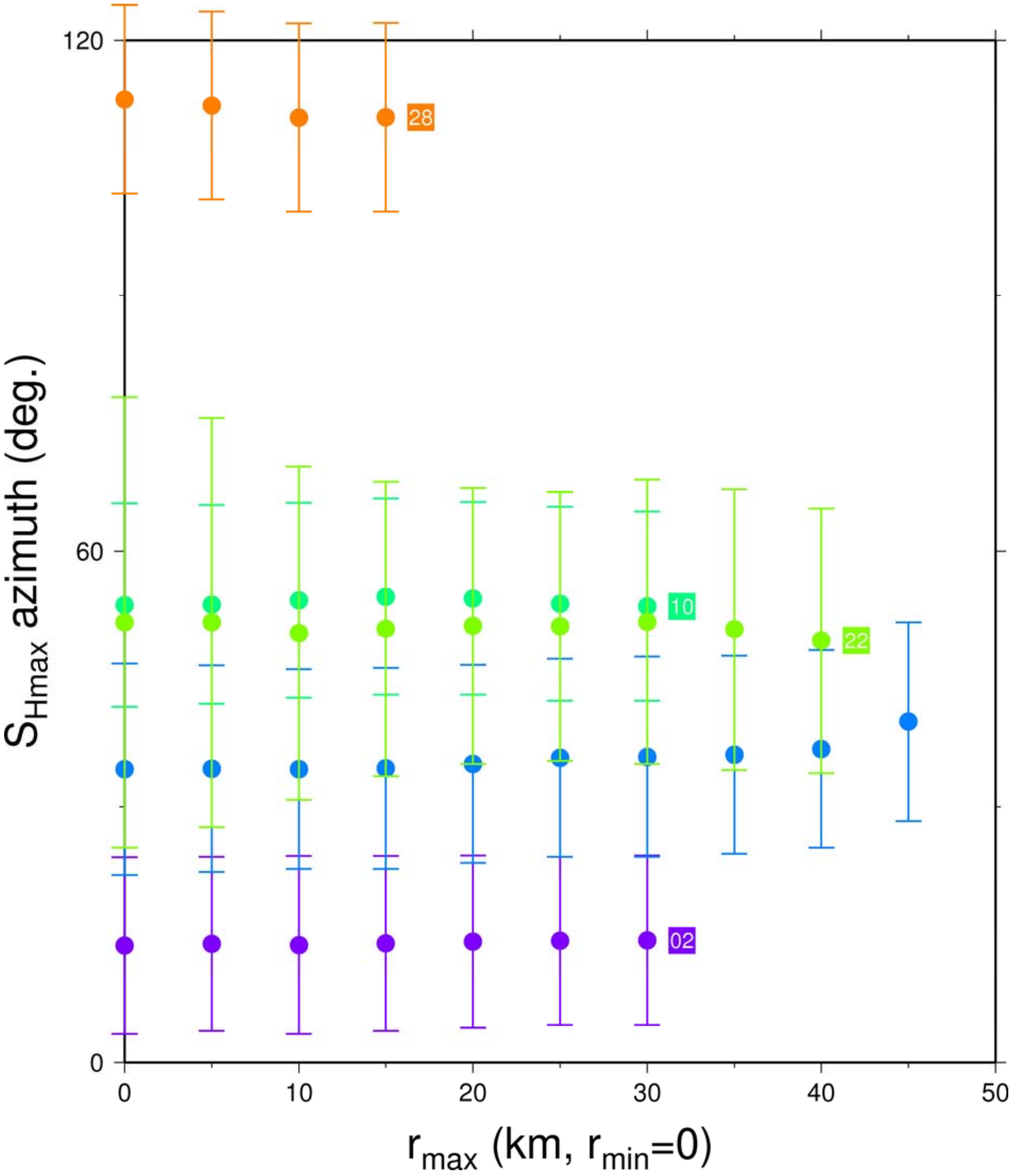

Figure 16 Illustration of the effects of different distance-weightings on the axis of maximum horizontal compressive stress. Earthquakes closer than r_{min} from the cluster centroid are assigned a weight of one; those earthquakes further than r_{max} from the centroid have a weight of zero; and those earthquakes lying between r_{min} and r_{max} are assigned weights of between one and zero based on a linear interpolation of distance. In this case r_{min} was fixed at 0 km.

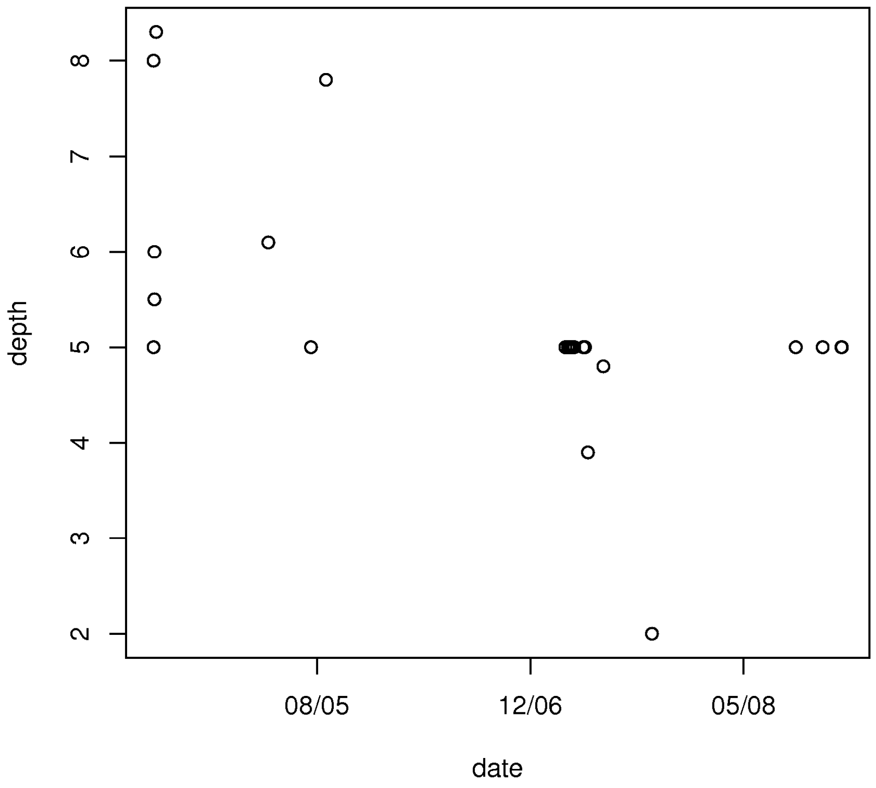

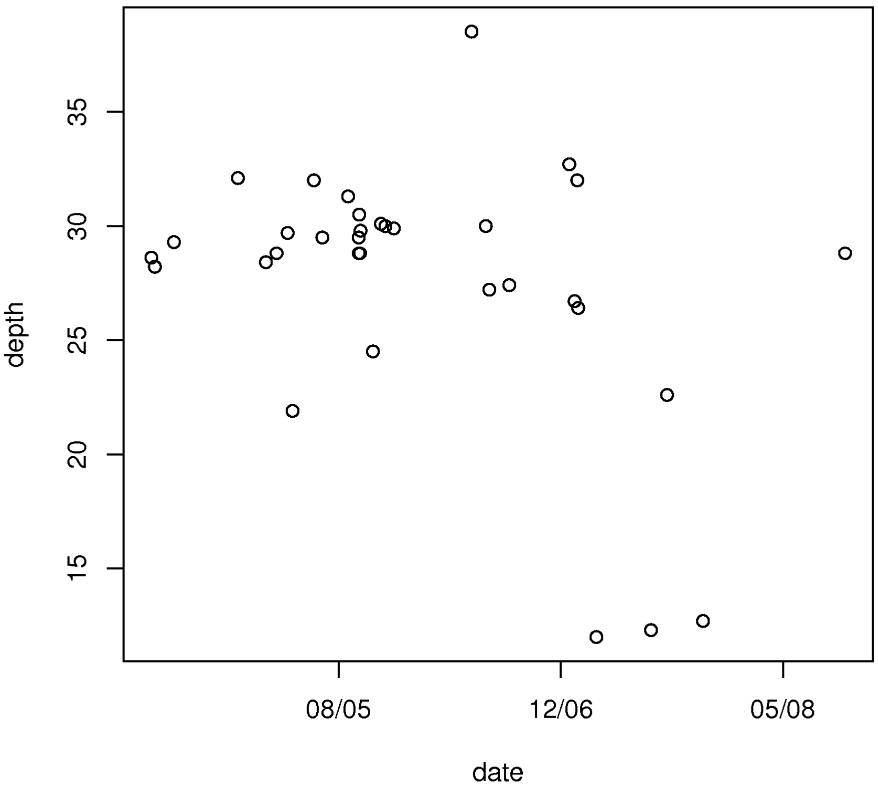

Figure 17 Focal mechanism depth plotted against time for clusters 3 and 10 from the 2D clustering. Note the change in typical depth for cluster 3: later earthquakes are deeper in general than earlier ones.

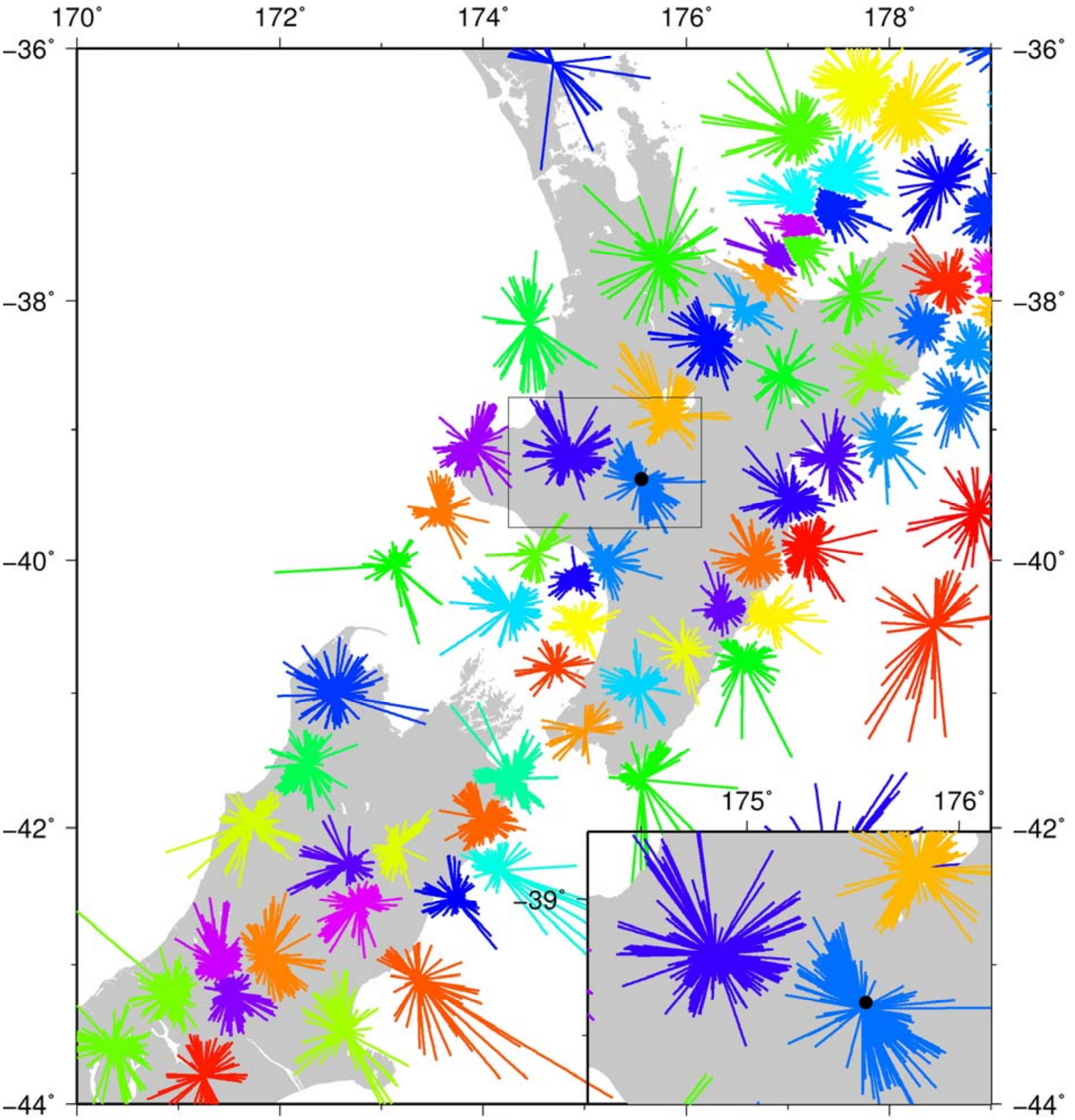

Figure 18 Clusters constructed from the long-term earthquake catalogue (~26,000 events; M>3, depth<25 km, January 1989 – December 2008). A line links each focal mechanism to its respective cluster centroid (i.e. the mean position for that cluster). Clusters were determined using k_{rot} = 114 and 50 iterations of the K-means algorithm.

TABLES

Table 1 Earthquake database search criteria.

Criterion	Value
Date	2004 - 2008
Search area	166 °E - 179 °E, 34 °S - 48 °S
Focal depth	≤ 50 km
RMS solution misfit	≤ 1.0
Azimuth gap	≤ 180 °
Number first motions	≥ 10

Table 2 2D clustering results; angles are in radians unless otherwise specified. The number of focal mechanisms is #FM, (ϕ,θ,φ) are the Euler angles of the principal axes of the stress tensor, and ν is the stress ratio. S_{Hmax} is the direction of maximum horizontal compressive stress, S_{Hmax} (10%) and (90%) are the lower and upper limits of an 80% credible interval for the S_{Hmax} direction. MOE (80%, °) is the half width (Margin of Error) of the credible interval (degrees).

Cluster	#FM	Lat.	Long.	ϕ	θ	φ	ν	S_{Hmax}	S_{Hmax} (10%)	S_{Hmax} (90%)	S_{Hmax} (°)	MOE (80%, °)
01	5	–39.15	174.51	3.75	2.73	0.71	0.39	1.40	0.92	–1.27	80	28
02	64	–39.52	175.70	3.39	1.60	1.57	0.59	0.25	0.08	0.42	14	10
03	26	–37.94	176.67	3.65	2.09	0.95	0.44	0.70	0.49	0.90	40	12
04	33	–41.58	174.22	5.12	1.84	1.70	0.58	1.96	–1.39	–0.96	113	12
05	7	–39.18	175.03	3.89	1.33	1.86	0.19	0.76	0.46	1.08	43	17
06	3	–43.05	171.12	4.71	1.82	2.11	0.72	1.53	1.21	–1.31	88	18
07	23	–40.92	174.59	1.07	1.46	4.44	0.52	1.05	0.86	1.24	60	11
08	44	–41.13	175.05	4.30	2.40	1.35	0.46	1.27	1.02	1.51	73	14
09	2	–37.57	177.67	3.36	1.14	2.45	0.31	0.55	–0.14	1.11	31	40
10	33	–39.31	175.08	0.92	2.19	4.67	0.59	0.93	0.74	1.13	54	11
11	27	–39.04	175.73	4.66	3.01	0.99	0.21	2.09	–1.25	–0.86	120	12
12	41	–39.13	175.38	1.88	1.68	4.48	0.46	1.89	–1.43	–1.08	108	10
13	13	–41.62	174.64	4.35	0.81	1.26	0.31	1.03	0.80	1.24	59	13
14	26	–40.87	175.54	0.32	2.94	3.84	0.54	1.16	0.96	1.35	66	11
15	5	–42.17	172.44	5.30	1.49	3.47	0.40	2.16	–1.44	–0.46	124	26
16	29	–40.10	174.99	1.29	1.66	4.45	0.45	1.30	1.11	1.48	75	11
17	11	–39.91	175.55	1.56	2.44	5.08	0.53	1.32	0.99	–1.51	76	19
18	33	–39.37	175.49	3.59	2.89	1.08	0.35	0.91	0.71	1.10	52	12
19	19	–39.84	176.76	3.29	0.88	1.85	0.42	0.28	0.08	0.47	16	11
20	8	–39.41	176.99	1.16	1.59	4.31	0.73	1.16	0.93	1.39	67	13
21	7	–42.35	173.85	1.69	0.99	3.42	0.64	1.62	1.33	–1.26	93	16
22	21	–40.39	176.13	1.54	0.65	3.87	0.19	0.86	0.59	1.13	50	16
23	21	–39.28	174.84	1.24	1.56	4.47	0.54	1.23	1.02	1.44	71	12
24	40	–38.87	175.95	2.60	2.94	6.16	0.33	1.16	0.96	1.36	67	11
25	17	–41.85	173.88	4.93	1.88	1.71	0.34	1.76	1.55	–1.18	101	12
26	5	–39.36	175.64	3.06	1.12	0.41	0.10	2.38	–1.17	–0.29	137	24
27	15	–39.59	176.29	1.13	1.77	4.39	0.43	1.17	0.97	1.36	67	11
28	42	–39.25	175.39	1.93	2.11	4.70	0.67	1.94	–1.40	–1.02	111	11
29	10	–38.50	177.34	1.04	1.49	3.67	0.68	1.01	0.78	1.25	58	13
30	3	–44.21	169.35	5.26	1.59	2.07	0.43	2.12	–1.44	–0.61	121	24

Table 3 3D clustering results; angles are in radians unless otherwise specified. The number of focal mechanisms is #FM, (ϕ,θ,φ) are the Euler angles of the principal axes of the stress tensor, and ν is the stress ratio. S_{Hmax} is the direction of maximum horizontal compressive stress, S_{Hmax} (10%) and (90%) are the lower and upper limits of an 80% credible interval for the S_{Hmax} direction. MOE (80%, °) is the half width (Margin of Error) of the credible interval (degrees).

Cluster	#FM	Lat.	Long.	ϕ	θ	φ	ν	S_{Hmax}	S_{Hmax} (10%)	S_{Hmax} (90%)	S_{Hmax} (°)	MOE (80%, °)
01	22	–40.14	174.95	1.08	1.65	4.32	0.46	1.09	0.90	1.28	63	11
02	23	–39.27	174.87	1.28	1.53	4.40	0.62	1.27	1.08	1.46	73	11
03	13	–41.10	174.50	4.20	1.78	1.63	0.50	1.05	0.85	1.24	60	11
04	27	–39.04	175.73	4.66	3.01	0.99	0.21	2.09	–1.25	–0.86	120	12
05	44	–39.35	175.50	3.40	2.80	0.87	0.45	0.88	0.68	1.07	50	12
06	15	–39.62	176.24	1.12	1.77	4.41	0.46	1.15	0.96	1.34	66	11
07	10	–38.14	176.54	3.77	0.87	1.64	0.34	0.66	0.38	0.93	38	16
08	10	–38.39	177.42	0.82	1.63	3.65	0.54	0.69	–0.08	1.20	40	44
09	17	–42.10	173.87	1.76	1.03	4.59	0.25	1.71	1.50	–1.23	98	12
10	8	–39.88	175.39	2.36	2.69	5.74	0.41	1.45	1.09	–1.35	83	21
11	6	–39.99	174.82	4.38	2.72	1.09	0.13	1.66	1.42	–1.25	95	14
12	18	–37.85	176.81	3.74	1.88	0.92	0.54	0.68	0.48	0.89	39	12
13	9	–40.96	175.04	2.02	1.52	4.82	0.55	2.02	–1.36	–0.89	116	14
14	15	–39.86	176.77	5.76	0.19	5.84	0.58	0.58	0.19	0.98	33	22
15	20	–40.88	175.62	0.22	2.94	3.78	0.57	1.12	0.88	1.36	64	14
16	37	–38.87	175.91	2.42	2.89	5.97	0.35	1.19	0.98	1.39	68	12
17	7	–40.53	175.11	3.35	0.22	2.31	0.23	0.92	0.67	1.17	53	14
18	5	–42.17	172.44	5.30	1.49	3.47	0.40	2.16	–1.44	–0.46	124	26
19	22	–40.38	176.15	1.57	0.68	3.75	0.18	0.78	0.55	1.01	45	13
20	7	–39.18	174.58	1.01	0.97	5.10	0.51	1.19	0.88	1.55	68	18
21	81	–39.18	175.37	1.88	2.05	4.69	0.64	1.88	–1.44	–1.09	108	10
22	3	–44.21	169.35	5.26	1.59	2.07	0.43	2.12	–1.44	–0.61	121	24
23	3	–43.05	171.12	4.71	1.82	2.11	0.72	1.53	1.21	–1.31	88	18
24	12	–39.50	176.90	1.22	1.50	3.81	0.73	1.21	0.97	1.44	69	13
25	31	–39.31	175.08	0.86	2.17	4.60	0.60	0.89	0.69	1.09	51	12
26	3	–38.81	176.41	4.22	1.61	1.57	0.35	1.08	0.75	1.42	62	19
27	50	–41.13	175.00	1.48	0.40	4.18	0.54	1.06	0.85	1.26	61	12
28	67	–39.53	175.70	3.39	1.61	1.57	0.59	0.25	0.08	0.42	14	10
29	20	–41.64	174.28	0.86	1.16	3.71	0.56	0.73	0.51	0.94	42	12
30	28	–41.62	174.22	5.22	1.64	1.58	0.39	2.08	–1.28	–0.85	119	12

Table 4 2D clustering results for earthquakes shallower than 25 km; angles are in radians unless otherwise specified. The number of focal mechanisms is #FM, (ϕ,θ,φ) are the Euler angles of the principal axes of the stress tensor, and ν is the stress ratio. S_{Hmax} is the direction of maximum horizontal compressive stress, S_{Hmax} (10%) and (90%) are the lower and upper limits of an 80% credible interval for the S_{Hmax} direction. MOE (80%, °) is the half width (Margin of Error) of the credible interval (degrees).

Cluster	#FM	Lat.	Long.	ϕ	θ	φ	ν	S_{Hmax}	S_{Hmax} (10%)	S_{Hmax} (90%)	S_{Hmax} (°)	MOE (80%, °)
01	28	–37.95	176.71	3.68	2.08	0.98	0.48	0.71	0.50	0.92	41	12
02	6	–42.28	172.27	1.99	1.64	2.84	0.47	2.00	–1.51	–0.72	115	21
03	15	–41.05	175.11	4.92	2.07	1.40	0.59	1.82	–1.55	–1.10	105	13
04	92	–39.19	175.36	1.77	2.10	4.71	0.61	1.77	–1.55	–1.20	101	10
05	27	–41.61	174.22	5.22	1.64	1.59	0.42	2.07	–1.28	–0.86	119	12
06	7	–40.14	176.51	5.35	1.97	2.70	0.47	2.10	1.50	–0.37	120	34
07	40	–38.87	175.95	2.60	2.94	6.16	0.33	1.16	0.96	1.36	67	11
08	15	–39.72	175.71	4.06	1.83	1.67	0.64	0.90	0.67	1.12	52	13
09	27	–39.04	175.73	4.66	3.01	0.99	0.21	2.09	–1.25	–0.86	120	12
10	5	–43.79	170.01	4.89	1.76	2.07	0.84	1.72	1.48	–1.18	98	14
11	15	–42.03	173.92	5.04	1.92	1.59	0.29	1.89	–1.45	–1.06	108	11
12	2	–39.82	173.74	4.42	1.70	0.97	0.44	1.31	0.85	–1.37	75	27
13	92	–39.45	175.61	3.86	0.52	1.00	0.42	0.29	0.10	0.47	17	11
14	25	–40.11	175.02	1.10	1.68	4.40	0.33	1.12	0.93	1.31	64	11

Table 5 Results for temporal stress change analysis. An estimate of the S_{Hmax} direction with an 80% credible interval is given for the total cluster (‘t’), and separate estimates after the cluster is split into early (‘1’) and late (‘2’) sequences. An estimate of the difference in S_{Hmax} (early-late) is given with a 95% credible interval. The margin of error (MOE) is the half width of the credible interval for ΔS_{Hmax}. All angles are in degrees.

Cluster	**Splitting date**	$S_{Hmax,t}$	$S_{Hmax,t}$ **CI**	**#FM$_1$**	$S_{Hmax,1}$	$S_{Hmax,1}$ **CI**	**#FM$_2$**	$S_{Hmax,2}$	$S_{Hmax,2}$ **CI**	$\Delta S_{Hmax,1-2}$	$\Delta S_{Hmax,1-2}$ **CI**	**MOE**
02	06/07/2007	14.3	(4.4, 24.1)	50	17.3	(6.5, 28.0)	14	0.2	(-12.1, 12.1)	17.1	(-7.9, 42.1)	25.0
03	01/06/2006	40.0	(28.4, 51.6)	8	-3.7	(-27.3, 19.9)	18	46.2	(34.0, 57.9)	-49.9	(-88.2, -11.1)	38.6
10	21/02/2006	53.6	(42.5, 64.6)	20	39.5	(27.7, 51.2)	13	74.4	(62.2, 86.1)	-34.9	(-60.4, -8.6)	25.9
22	01/05/2008	49.5	(34.0, 64.6)	13	48.4	(31.9, 64.3)	8	40.7	(24.5, 56.9)	7.7	(-32.9, 44.9)	38.9
28	01/01/2006	–69.0	(-80.1, -58.3)	21	-58.9	(-70.6, -47.7)	21	101.3	(81.9, 118.2)	19.8	(-10.7, 52.3)	31.5

www.gns.cri.nz

Principal Location

1 Fairway Drive
Avalon
PO Box 30368
Lower Hutt
New Zealand
T +64-4-570 1444
F +64-4-570 4600

Other Locations

Dunedin Research Centre
764 Cumberland Street
Private Bag 1930
Dunedin
New Zealand
T +64-3-477 4050
F +64-3-477 5232

Wairakei Research Centre
114 Karetoto Road
Wairakei
Private Bag 2000, Taupo
New Zealand
T +64-7-374 8211
F +64-7-374 8199

National Isotope Centre
30 Gracefield Road
PO Box 31312
Lower Hutt
New Zealand
T +64-4-570 1444
F +64-4-570 4657